DISSERTATION

CONSTRAINING SATELLITE PRECIPITATION BIASES THROUGH GEOPHYSICAL ARGUMENTS

Submitted by

Eric Goldenstern

Department of Atmospheric Science

In partial fulfillment of the requirements

For the degree of Doctor of Philosophy

Colorado State University

Fort Collins, Colorado

Fall 2025

Doctoral Committee

Advisor: Christian Kummerow

Christine Chiu
Kristen Rasmussen
Imme Ebert-Uphoff

ABSTRACT

CONSTRAINING SATELLITE PRECIPITATION BIASES THROUGH GEOPHYSICAL ARGUMENTS

Passive microwave satellite precipitation products provide crucial information on global rainfall and the only source of such information over much of the world. These products operate under the assumption that microwave brightness temperatures (TBs) are sufficient to constrain rainfall. This information, however, often represents multiple rain states, resulting in substantial and highly variable errors. Consequently, substantial regional biases can exist that are related to how well these assumptions characterize the actual precipitation. Traditional error analyses use a reference precipitation dataset, often from rain gauges or radars, which are only available in limited portions of the world and can only represent the areas in which they operate. As such, much of the world is left without an objective quantification of satellite precipitation errors. The work of this dissertation aims to address this gap in coverage by determining alternate methods by which errors can be estimated.

To characterize these potential error sources and their effects, coincident GPROF Version 7, Global Precipitation Measurement (GPM) Microwave Imager (GMI), and GPM Combined observations, which closely mirror the GPM radar products, were examined over three tropical land regions known to exhibit distinct biases relative to one another. The interrelation between rain rate and ice-rain ratio (IRR) was identified as the primary descriptor of regional bias, which accounts for roughly 50% of the observed GPROF biases. Accounting for surface effects further improves this, accounting for roughly 70% of the observed biases when considered with rain rate and IRR. Comparing the effects of these three parameters between GPROF Version 7 and the 1-D version of GPROF-NN showed similar improvements, indicating the utility of this error attribution across precipitation products.

From the three error sources identified, both rain rate and surface effects can be classified using radiometer information, but IRR requires the infrequent radar overpasses and therefore is not always available. Since the formation of atmospheric ice should be driven by the incident environment, an investigation on this linkage was undertaken. Seven years of spaceborne radar and precipitation measurements from GPM taken over three tropical land regions were obtained to investigate this hypothesis. Five ice content regimes, as defined by ice rain ratio (IRR), were identified and found to relate to distinct precipitation regimes. These regimes were coupled with CAPE, TCWV and Tavg information from ERA5, which proved to both reproduce the spatiotemporal characteristics of the regimes and their effects on regional bias constraint. These effects appear largely unaffected by shifts in the input data and time series, showing that the environments in which certain precipitation regimes occur are generalizable to other locations and times.

Having established the sources of error in passive microwave precipitation products and the ability of the large-scale environment to diagnose these sources, a method for quantifying these errors using ERA5 information was developed. This framework, termed the Satellite Precipitation Errors from Ancillary Data (SPREAD) model, utilizes support vector regression to directly predict product errors from the retrieval rain rate and ERA5 thermodynamic and kinematic information. Evaluations of SPREAD show promise in developing error estimates in the Tropics, where it was trained, while further work is needed to improve its ability to predict errors in regions outside of the Tropics. Investigations of the resolution sensitivity on the model indicates that SPREAD is most stable when assessing precipitation errors at large scales, reflecting the resolution capabilities of the ERA5 data. Though a prototype, the SPREAD model shows the capability of attributing satellite precipitation retrieval errors in cases where traditional validation analyses are not possible by leveraging information provided by the large-scale meteorological conditions.

ACKNOWLEDGEMENTS

First and foremost, I would like to thank my advisor, Dr. Christian Kummerow, for his continued support over the six years I have worked toward this degree. Your insights and advice on research, academia and life in general have been instrumental in shaping me as a scientist and a member of society. I would also like to thank my committee members, Drs Christine Chiu, Kristen Rasmussen and Imme Ebert-Uphoff for their continued support throughout my time here at CSU. You all have contributed valuable insights and expertise as I have pursued my work, and I could not be more thankful for the work that you all have done.

Thank you to all members of the Kummerow research group, both past and present. Every one of you has had an impact on my research and life and I wish every single one of you the best in your future endeavors. Thank you to the entirety of the students, faculty and staff of the Department of Atmospheric Science here at CSU. I chose CSU because of the community we all foster, and I cannot be more appreciative of all of you for maintaining this atmosphere of academic excellence and camaraderie.

Finally, thank you to all my friends and family, both in and outside Colorado, that have supported me throughout my studies. Everyone is a product of their environments, much like the weather, and I am so grateful that the environment you provided me has allowed me to flourish as a scientist and as a person. A special thank you is in order for my partner Abi, who has been my biggest cheerleader in the lead up to the completion of my degree and the beginning of my career in academia.

The research in this dissertation was supported by the NASA PMM Awards 80NSSC19K0680 and 80NSSC22K0604.

TABLE OF CONTENTS

CHAPTER 1: INTRODUCTION

1.1 Motivation

Precipitation is an integral branch of the hydrologic cycle and is responsible for redistributing fresh water across the Earth. In reasonable proportions precipitation allows terrestrial life to flourish but can be quite destructive in the wrong amounts. Too little precipitation results in drought and desertification, which alongside warming temperatures negatively impacts agricultural yields (Kuwayama et al. 2018; Madadgar et al. 2017) and increases the risk of wildfires (Richardson et al. 2022). Too much precipitation results in flooding which remains one of the deadliest and most costly weather-related hazards (Fatorelli et al. 1999; Pielke and Downton 2000). The frequency and intensity of precipitation events are expected to be modified considerably in response to the warming climate, further compounding the effects of these hazards (IPCC 2023). Given the precious commodity that fresh water is, its destructive potential and the ongoing and anticipated changes in the hydrologic cycle due to climate change, it is tantamount to society to properly quantify precipitation.

Measuring precipitation is an activity nearly as old as civilization itself. Recorded rainfall measurements date back as far as the fourth century BC (Strangeways 2010) and have continued in many different aspects through to the modern era. All methods of precipitation measurement fall into two categories: in-situ and remotely sensed. In-situ precipitation measurements, like those made by rain gauges, directly interact with precipitation to make their assessments. Remotely sensed measurements, like those from radars and satellites, can assess precipitation from a distance and thus do not require contact with it. Each of these techniques has its own advantages and disadvantages. In-situ measurements require continual calibration and support to remain usable and suffer from evaporation and wind displacement issues (Cauteruccio et al.

2021; Kochendorfer et al. 2017; Leeper and Kochendorfer 2015), making nonlocal assessments of precipitation from these platforms challenging. Remotely sensed measurements can largely circumvent the areal coverage issues prone to in-situ measurements, but they do not directly measure precipitation. Rather, they relate precipitation to another information source that can be assessed from a distance, such as microwave pulses for radars or passive radiation for satellites. As such, these observations must be ingested by a forward model to produce precipitation estimates, which can introduce errors through forward model uncertainties and non-uniqueness (Michaelides et al. 2009; Stephens and Kummerow 2007).

Many satellite precipitation products have been developed using the radiative information gathered by radiometers and sounders across the electromagnetic spectrum. The most useful of these products incorporate microwave information, which is more sensitive to the hydrometeors present in a cloud and hence provide more direct knowledge of the precipitative capacity of a system. Microwave radiation predominantly interacts with cloud hydrometeors through absorption and scattering. Absorption and emission are typical of liquid water droplets and water vapor at low and very high frequencies respectively, while scattering is a property of ice particles at high frequencies. By assessing multiple frequencies, passive microwave satellites can provide a considerable amount of information on the hydrometeor characteristics of a precipitating system, allowing for greater insight on the precipitation being produced (Spencer 1986; Vivekanandan et al 1991; Wilheit 1986). This information, however, does not uniquely determine precipitation, and as such these products exhibit noteworthy errors across multiple scales. This presents a challenge particularly in data-sparse regions, where these products are often the only source of information for rainfall (Gebregiorgis and Hossain 2014). As such, understanding these errors is of great importance for accurate global assessments of precipitation from satellites.

1.2 Filling the Gaps in Traditional Error Assessment Techniques

Error assessment for satellite precipitation products typically occurs through ground validation studies. These studies utilize a well-calibrated "ground truth" dataset which is compared to the desired product to develop its error characteristics. An example of such a study is the GPM Ground Validation Program (Petersen et al. 2020), which utilized information primarily from the Continental United States to quantify errors in precipitation from the Goddard Profiling Algorithm (GPROF; NASA 2022). While these studies remain the most accurate method for determining satellite precipitation errors, they are limited to the region in which they occur and do not generalize well outside of it. This is primarily due to the lack of correspondence between different regions in terms of the precipitation systems present, even if those regions exhibit similar overall precipitation characteristics. For data-sparse regions, this lack of information transferability results in a near-complete lack of definable error information. Other methods like product intercomparisons can somewhat alleviate this problem but are also sensitive to the assumptions made by the individual algorithms and thus may not accurately represent the errors present (Adler et al 2012). As such, a method which can be generalized outside of its training region and utilizes information which can emulate errors accurately and in an explainable manner is desired to bridge the gaps in global error analysis.

This dissertation aims to provide the framework by which error characterization for satellite precipitation products can be achieved in the absence of traditional validation techniques. While the atmosphere is a highly chaotic system, it does follow general rules which dictate the formation of clouds and precipitation (e.g. Chen et al. 2004; Del Genio and Kovari

2002; Hsiao et al. 2024; Nielsen and Schumacher 2020; Schiro et al. 2020). As such, understanding the occurrence of these rules and relating them to the information which can be gathered by satellites would thus provide error estimates which can be developed using globally available information and is physically linked to the processes and assumptions innate to satellite precipitation products. Such a framework would be generalizable on account of its reliance on the environment as opposed to specific locations and times and provide actionable error information in the data-sparse regions. With the length of the satellite data record also approaching the scale necessary for climatological analyses, the application of these errors would also be advantageous for the assessment of precipitation characteristics as they respond to climatic forcings. In short, this dissertation provides a basis by which to provide more consistent and reliable satellite precipitation products to assess global precipitation at multiple scales.

1.3 Outline

This dissertation is composed of five total chapters. Chapter 1 is this introduction, in which the background and motivation for the following body of work is presented. Chapters 2 through 4 describe the research data, methods and results which have been accomplished in completion of this dissertation. Each of these chapters has either been published in peer-reviewed journals or is in preparation for such. Chapter 2 establishes the physical links between the radiative theory used by passive microwave satellite precipitation products and radar-derived hydrometeor information which can constrain regional errors. Chapter 3 relates the observed ice hydrometeor characteristics to environmental conditions, establishing the link between the large-scale meteorology and the constituents which drive errors. Chapter 4 combines this information to predict errors directly from environmental information. Chapter 5 presents a summary of the previous chapters.

CHAPTER 2: UNDERSTANDING REGIONAL PASSIVE MICROWAVE PRECIPITATION BIAS USING RADAR-DERIVED INFORMATION[1]

2.1 Introduction

Precipitation is an essential aspect of the Earth system owing to its role as a controlling factor in the global water and energy cycles. Much of this information is obtained from spaceborne platforms, which circumvent many of the issues confronted by ground-based measurements such as terrain blockage and inhomogeneous spacing (Villarini et al. 2008; Vivekanandan et al. 1999). Precipitation is also a highly variable process, occurring at very fine spatiotemporal scales (Krajewski et al. 2003) and with high sensitivity to many difficult-to-quantify environmental characteristics. This variability results in uncertainties which then have downstream impacts on climate records of precipitation and in operational product fidelity. These uncertainties exist both globally and regionally, which further complicates their interpretation from ground validation sites. Given the necessity to provide the most accurate assessments of precipitation possible, efforts to quantify random and systematic uncertainty remain at the forefront of precipitation research.

To date, most uncertainty quantification methods come in the form of either ground validation studies or product intercomparisons. Ground validation studies, which utilize direct comparisons between a high-quality “ground truth” dataset and the precipitation product in question, have served as the backbone for product assessment in most precipitation measurement endeavors. Some examples of this work are detailed in Hossain and Anagnostu (2006), Maggioni et al. (2014) and Petersen et al. (2020). These studies, however, are typically performed at local to regional scales, meaning they do not necessarily represent the uncertainties in other areas

---

[1] **Published as:** E. M. Goldenstern and C. D. Kummerow, "Understanding Regional Passive Microwave Precipitation Bias Using Radar-Derived Information," in *IEEE Transactions on Geoscience and Remote Sensing*, vol. 62, pp. 1-9, 2024, Art no. 4110509, doi: 10.1109/TGRS.2024.3470552.

(Dezfuli et al. 2017; Maghsood et al. 2017; Pfreundschuh et al. 2024). This is most impactful for developing areas, where these products are most urgently needed due to the lack of reliable ground observations (Gebregiorgis and Hossain 2014). Precipitation product intercomparisons, in contrast, determine the systematic errors of a given product relative to the dispersion of an ensemble of related products (Smith et al. 2006, Adler et al. 2012). While more readily applied to global precipitation records, such intercomparisons represent errors in terms of statistics as opposed to physics, which can result in significant underestimates or overestimates of uncertainty when the product ensemble makes similar but incorrect assumptions across all members.

More recently, efforts to relate uncertainty to specific kinematic and thermodynamic processes have garnered increased attention. One example focused on climate scale tropical ocean precipitation is from Leitmann-Niimi (2023). This study found that water budget closure, defined as a balance of water vapor divergence, evaporation, and precipitation, is mostly affected by precipitation errors that can be related to convective organization and various teleconnection patterns. Another study by Petkovic and Kummerow (2017) looked at regional biases in the Goddard Profiling Algorithm (GPROF) over two tropical land regions. Here, it was found that some large-scale thermodynamic and kinematic parameters like convective available potential energy (CAPE) and surface dewpoint depression showed some utility in characterizing certain precipitation processes that may be related to retrieval biases. Other studies have also indicated that the large-scale environment is capable of influencing precipitation errors through modification of various related parameters and processes (Berg et al. 2006; Derin and Kirstetter 2022; Goldenstern and Kummerow 2023).

While the above uncertainty quantification methods have been put forward to describe precipitation uncertainties, none have attempted to determine the parameters which directly affect the observed brightness temperatures (TBs) used by satellite precipitation algorithms to diagnose precipitation, and therefore its biases. Since these TBs carry information related to vertical hydrometeor structure, which can be gathered from radar observations, an opportunity is provided to determine which hydrometeor characteristics are most influential to regional biases. Therefore, it is hypothesized that regional precipitation biases can be explained and accounted for by identifying the primary hydrometeor information which controls these TBs. This information would also provide a pathway by which various kinematic and thermodynamic processes can be related to precipitation estimates, eventually allowing for the diagnosis of bias at various scales. While this study's analyses are focused on Version 7 of GPROF (hereafter GPROF; NASA (2022)), it is believed that in other algorithms which use similar TB information, these structures will act similarly and thus produce roughly consistent behaviors.

This chapter is organized as follows. Section 2.2 describes the data and GPROF retrieval procedure used in this study. Section 2.3 describes the identification of the primary radar-derived hydrometeor characteristics which can explain retrieval bias. Section 2.3 also describes efforts to further improve this explanation by investigating potential second order effects. Section 2.4 describes efforts to extend these results to another passive microwave retrieval algorithm. Section 2.5 provides a discussion of the results from the body of the chapter.

2.2 Data and Methods

2.2.1. GPROF Precipitation Retrieval and a-priori Database

This study employs GPROF as the target precipitation product, which utilizes passive microwave information from the Global Precipitation Measurement (GPM) Mission satellite constellation to generate globally available precipitation estimates. While GPROF was selected for this study, it merely serves as an example for other passive microwave retrievals which would behave similarly. This algorithm relies on Bayes' theorem, utilizing an a priori database of microwave TBs and ancillary data like surface temperature to compare against observed conditions. These comparisons are used to develop weights for the database entries, which are then combined in a weighted average to create a posterior precipitation rate estimate. The GPROF a priori database is comprised of information gathered from October 2018 to September 2019 from the GPM Combined Radar-Radiometer Algorithm (CMB; Grecu et al. 2016), which uses an optimal estimation approach to blend information from the GPM Microwave Imager (GMI) and Dual Precipitation Radar (DPR) and generate physically consistent precipitation estimates. This database will also comprise the data utilized in the subsequent analyses. Both the GPROF and CMB data are available from the NASA PMM group (https://pps.gsfc.nasa.gov).

2.2.2. GPM Combined Hydrometeor Information

To determine the effects of various sources of hydrometeor information, the rain and ice water profiles from GPM Combined were used. These profiles provided water contents at 500 m resolution from the surface to 10 km above ground level and 1000 m from 10 to 18 km. Since these profiles are utilized in the development of GPROF's a priori database, they are already at the GPROF resolution, simplifying their use. It is also worth noting that these hydrometeor profiles and any information gathered from them are only available along the DPR swath, so the results to be presented are only valid for this collocation and not the full operational GPROF swath.

Before these rain and ice water profiles were used in the subsequent analyses, some modifications were performed to improve the physical consistency between the radar and TB observations. Due to differences in the scan geometry between DPR (nadir-pointing) and GMI (52° incidence), the water content profiles were matched to the footprint location in the scan line immediately preceding a given GPROF footprint. This was done to better align the profiles with the TBs used by GPROF in its estimates. The profiles were also adjusted within a 2-km deep layer centered at the freezing level using a linear decay for rain and a linear growth for ice to reduce the effects of bright banding.

From these profiles, characteristics such as water path and layer water content were developed. The path variables (Path) were calculated as a summation between the product of the individual level water contents (WCi) and the distance between that level and the previous one (dzi) through the entire profile extent (j = 28 levels), as shown in (2.1). Layer water content (WCLYR) was defined as the sum of the individual level water contents within a given depth (L), as shown in (2.2)

$$Path = \sum_{i=1}^{j} WC_i * dz_i \tag{2.1}$$

$$WC_{LYR} = \sum_{i=1}^{L} WC_i \tag{2.2}$$

2.2.3. Retrieval Setup and Uncertainty Quantification Method

Since this study is focused on regional variability in uncertainty, GPROF was run in an experimental mode where it was tasked to predict on its own database. The advantage of this mode is that it focuses on the algorithm’s deficiencies by utilizing a known truth in the database rain rates rather than ground validation data, which often has its own set of issues when comparing different locations. The database used in this mode was restricted to three regions of interest (ROIs) within the Tropics (see Fig. 2.1) and to entries associated with the GPROF max vegetation (class 3) and mountain rain (class 17) surface classes to minimize the variability introduced by different climatic regimes and surface conditions. As such, the following analyses and results are the first steps toward explaining bias and are likely not suited for global application. The ROIs chosen include the Amazon (AMZN), Congo (CNGO), and Southeast Asia (SEAS). AMZN and CNGO were defined identically to Petkovic and Kummerow (2017), while SEAS was selected as an additional test region at 5–25 N; 90–110 E. These regions represent tropical landmasses which experience large amounts of annual rainfall but are known to have different biases in GPROF.

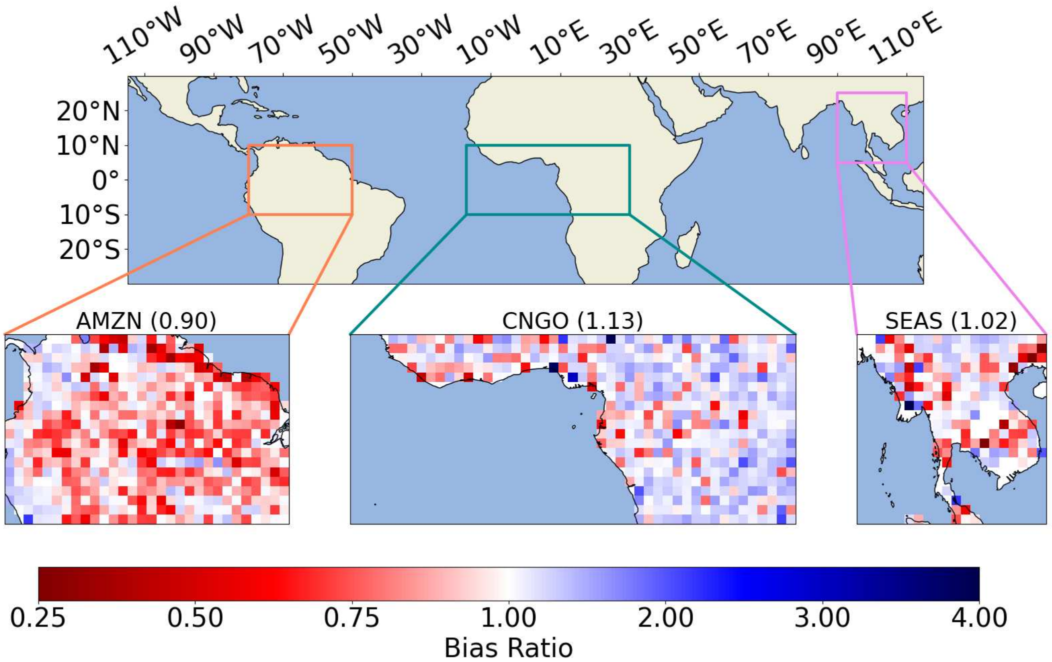

Fig. 2.1. Three ROIs were utilized in this study. The values in parentheses are the ROI mean bias ratios, while the colored grids are the 1◦ ROI bias ratios.

The metric chosen to quantify biases was the bias ratio. As shown by (2.3), this metric represents the ratio of the accumulated precipitation from the retrieval ($\Sigma GPROF$) to the accumulated precipitation from the truth dataset ($\Sigma refRR$). This accumulation is performed over two different volumes: the entire regional subset and within 1◦ × 1◦ areas within each ROI.

$$Bias\ Ratio = \frac{\Sigma GPROF}{\Sigma refRR} \tag{2.3}$$

Though CMB is itself an estimate, it is radar-derived and therefore closer to an objective truth than GPROF, particularly over land where PMW information content is lower. Previous studies have also indicated satisfactory correspondence between CMB and ground radar measurements, further signaling its credibility as a truth dataset (Biswas and Chandrasekar 2018, Olson et al. 2023). Future studies would look to use ground observations in place of GPM Combined. When calculating the bias ratio, only entries where the CMB rain rate in the study database was between 0.25 and 32 mm/hr were used. This range represents 95% of the accumulated rainfall, removing the effects of extreme precipitation on the subsequent analyses. Bias ratio values less than 1 represent underestimation by GPROF and greater than 1 overestimation.

Another benefit of using a bias ratio is that it can be inverted to remove the associated bias from GPROF through a simple multiplication of the two. Such an adjustment allows for both an objective quantification of bias and a method by which to determine the contribution of a specific phenomenon to the overall systematic bias. Initially, this adjustment was used to scale the regional GPROF database to ensure it was unbiased overall. This choice was made to ensure that focus was given to the regional discrepancies as opposed to artificial biases introduced by restricting the database.

2.3 Results

2.3.1. Initial GPROF Regional Bias Analysis

By design, GPROF is unbiased globally when compared against GPM Combined, so the regional bias characteristics were considered. To investigate these biases, two sets of bias ratios were developed for each region: an overall bias using the full set of ROI data and 1◦ gridded bias ratios using the ROI data contained by each grid space. Fig. 2.1 displays both perspectives. In the overall biases, the Amazon and Congo exhibited obvious systematic differences consistent with Petkovic and Kummerow (2017), being 0.9 (10% underestimation) and 1.13 (13% overestimation), respectively. Southeast Asia exhibited the lowest overall bias at 1.02 (2% overestimation). In aggregate, the three ROIs occupy a bias range of ±13%, highlighting the large regional discrepancies in uncertainty. At 1◦ resolution, additional context for these differences can be observed. In the Amazon, broad underestimation across the region was observed, with the northeastern coastline and rainforested portions comprising the strongest tendencies. This was contrasted by the area near the Andes Mountains, which showed a consistent overestimation tendency. The Congo, however, was broadly overestimated, especially in the eastern portion of the region. Some underestimation was also observed primarily along the West African coastline. In Southeast Asia, considerable spatial variability was apparent, likely contributing to the low overall bias. In general, the mountainous areas of the region showed the most coherent overestimation pattern alongside underestimation in the coastal lowland areas.

The spatial distribution of bias within the regions also provides clues for the hydrometeor characteristics which may be relevant. The underestimated areas within AMZN, for example, typically experience precipitating systems initiated by coastal squall lines, which due to the maritime nature of the associated airmass are often shallow and dominated by warm-phase microphysics (Cohen et al. 1995). Along the Andes, however, deep convection is often the source of precipitation and has a much stronger signature in the higher frequency microwave data. In general, CNGO is well-known for having some of the most vigorous deep convection in the world, driven largely by the African Easterly Jet and orographic enhancement from the Ethiopian Highlands. The coastal region, however, is strongly influenced by both the location of the Intertropical Convergence Zone (ITCZ) and the West African Monsoon, both of which display more maritime characteristics (Dyer et al. 2017). SEAS encompasses a topologically and climatologically complex area, with seasonal impacts from the Asian Monsoon and Madden–Julian Oscillation (MJO) interacting with the Annamite and Luang Prabang mountain ranges (Wang and Chang 2012), often resulting in enhanced deep convection along these mountains and stronger maritime influences over the lowland and coastal areas of the ROI. These comparisons indicate that differences between the regions relate to the predominant microphysical regime at play, which would be captured both by the microwave TBs used in GPROF and the hydrometeor characteristics from GPM Combined.

2.3.2. Main Constraint Identification and Partitioning

Having identified GPROF's regional bias variability, an assessment of the causes of these biases was undertaken. The first and most obvious cause relates to the GPROF architecture itself. As a Bayesian algorithm, GPROF creates an average state by combining multiple database entries with similar TBs and develops its precipitation estimate as a weighted average of these states. This simplistic methodology forces the GPROF estimates toward the mean of the a priori database, causing overestimation at low rain rates and underestimation at high rain rates, as shown in Fig. 2.2. This also explains why GPROF is unbiased overall, as the bulk of the precipitation accumulation histogram in Fig. 2.2 resides in rain rates which were relatively unbiased when taken in aggregate. This suggests that the rain rate can be used as a bias diagnostic.

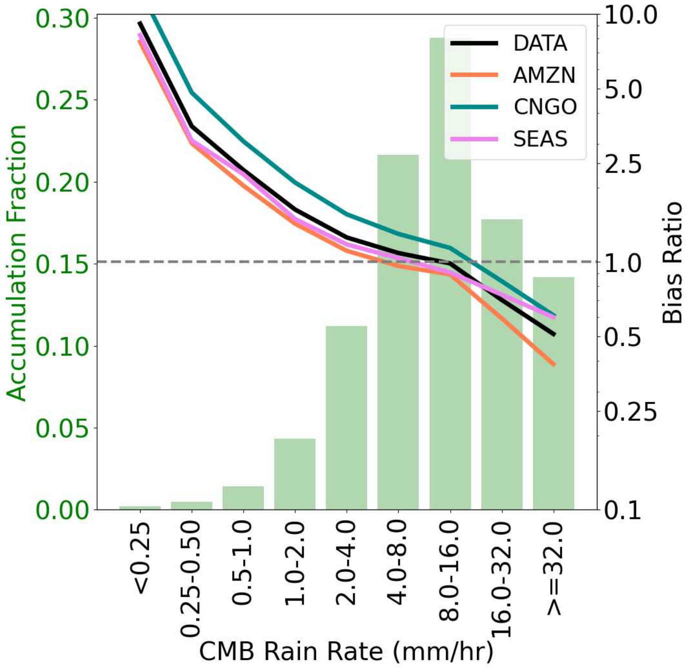

Fig. 2.2. Rain rate accumulation histogram (green bars) and associated bias ratios for the regional database (black), Amazon (orange), Congo (cyan), and Southeast Asia (violet).

Instead of using surface rain rate to examine this potential bias source, this study utilizes a reference rain rate (refRR), determined using the GPM Combined rain water content from a 1-km deep layer centered 1.5 km below the freezing level (refRWC). This choice was made for multiple reasons. First, CMB suffers from ground clutter and thus produces a near-surface rain rate from the lowest clutter-free bin which can vary in distance from the surface. In addition, environmental factors such as evaporation can modify rainfall, making the surface rain rate less representative of the precipitative capacity of the system. Using refRR provides a consistently located quantity which is more representative of the underlying precipitation processes. Equation (2.4) details how refRR is calculated from refRWC using information regarding the Marshall–

Palmer distribution (Marshall and Palmer 1948) and raindrop fall velocities. Here, refRWC has units of g/m−3 and refRR has units of mm/hr. This conversion serves to interpret biases in terms of rain rate and does not impact any results.

$$refRR = 17.87 * refRWC^{1.19} \tag{2.4}$$

In addition to substituting surface rain rate for refRR, the distribution of rain water between the reference level and the surface, hereafter referred to as rain profile slope or RRslope, was considered as an additional rain-dependent cause of bias. This choice was made to better determine if near-surface effects like evaporation have a notable impact on bias. RRslope was determined in (2.5) as the percent change between refRWC and a near-surface rain water content (sfcRWC) determined using the 1-km layer closest to the surface. In cases where RRslope indicated preferential water collection at the reference level (high-positive slope), one would expect overestimation to occur and vice versa where the distribution preferentially collected water near the surface (high-negative slope) owing to the differences between the reference and surface precipitation

$$RRslope = \frac{refRWC - sfcRWC}{sfcRWC} \tag{2.5}$$

The passive microwave TBs used by GPROF provide another clue for explaining bias. Because the surface emissivity over land is very high, the liquid emission signal from cloud and rain hydrometeors is heavily obscured, leaving the ice scattering signal as the largest source of information. This is best observed in high-frequency PMW channels like the 89- and 166-GHz channels in GMI, where TBs are reduced as scattering increases (Adhikari et al. 2019; Mohr and Zipser 1996). This information is often associated with increased precipitation, so GPROF assigns higher precipitation values to these conditions. Ice scattering, however, is more strongly influenced by cloud microphysical processes than precipitation processes and need not represent actual changes in rainfall. As a result, the precipitation rate is often overestimated in GPROF footprints with large amounts of ice and underestimated in those with little to no ice. This effect also couples with rain intensity, since a given rain rate can be associated with multiple ice amounts. As such, the amount of ice water with respect to the amount of rain water, here defined as the ice–rain ratio (IRR), is another potential cause of bias. For this study, IRR was defined in (2.6) as a ratio between the ice water path from 1.5 km above the freezing level upward (IWP) and refRWC

$$IRR = \frac{IWP}{refRWC} \tag{2.6}$$

Fig. 2.3 shows how the bias ratio varies by IRR. As IRR increased, the bias ratios shifted from underestimation to overestimation. This behavior broadly supports the underlying theory that clouds with greater amounts of ice are linked to higher precipitation values, as discussed by Braga and Vila (2014). The underestimation at lower IRR values also highlights well-known issues in GPROF for representing warm-phase precipitation (2012). This relationship between IRR and bias ratio also showed sensitivity to rain intensity, with the highest rain rates remaining underestimated at large IRR values while low rain rates were overestimated at low IRR values, as depicted by the different lines in Fig. 2.3. This indicates that IRR should be used alongside rain intensity to explain bias.

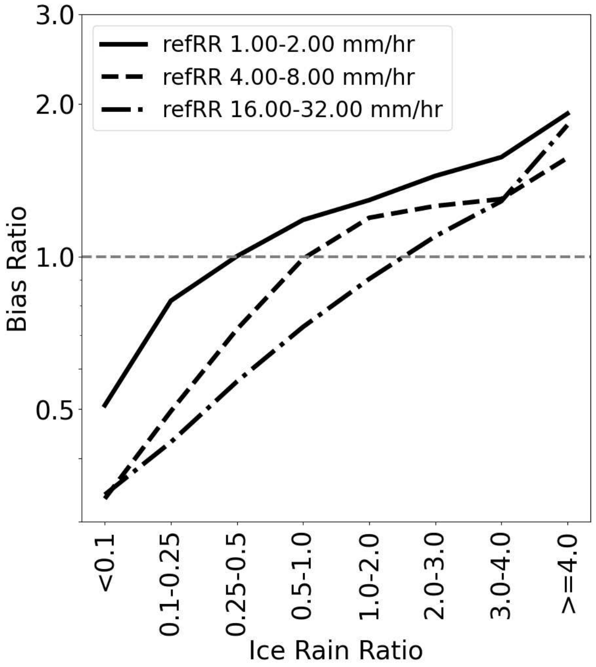

Fig. 2.3. Bias ratio as a function of IRR. Each line represents the data attributed to varying rain intensities.

To look at how these parameters can explain GPROF biases, the precipitation data were grouped based on refRR and IRR. These bins were determined by hand for refRR (0.25 and 32 mm/hr) and IRR (0.1 and 4). The bin intervals were first created using the smallest possible number of partitions which were believed to capture similar conditions. If a given bin experienced a notable decrease in the standard deviation of bias when split in half, these new bins were retained. Care was also taken to ensure the bins were sufficiently populated (1000+ entries). This resulted in nine refRR and eight IRR bins. The terciles of the rain profile slope were later used as an additional constraint. Fig. 2.4 displays these groups and their associated bias ratios. From this figure, several conclusions can be drawn regarding GPROF's bias tendencies. Both the behaviors discussed regarding bias ratio as a function of rain rate and ice amount are clearly visible. As IRR increases, the overestimation bias is extended into the moderate refRR bins, representing the effects of ice scattering. Once refRR is sufficiently large, the underestimation tendency dominates even at high IRR values, showing the importance of the rain rate effects.

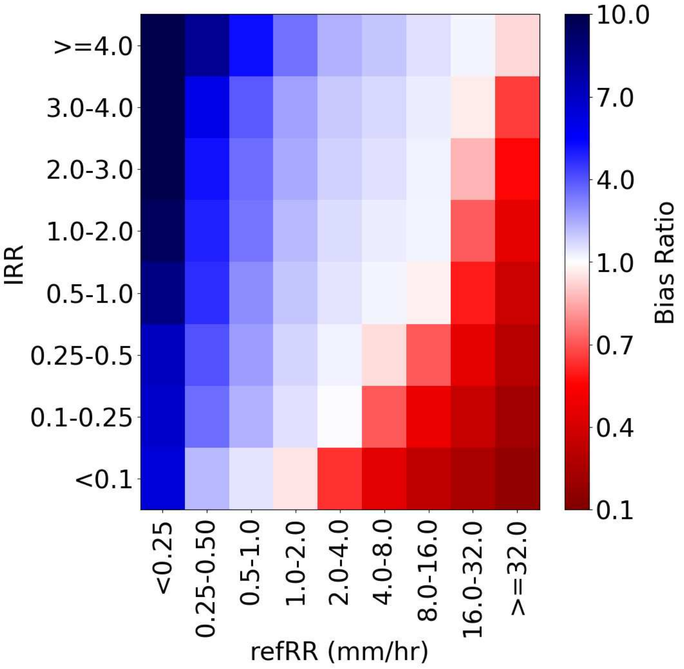

Fig. 2.4. Bias ratios for each of the 72 refRR-IRR groups. These ratios are determined as the mean ratio for each group.

The bias ratios shown in Fig. 2.4 were then inverted and used to adjust the GPROF rain rates associated with each reference rain—IRR group. By using this adjustment, a residual bias was created and compared to the original bias. If these two parameters can fully explain the bias, then this residual would show an unbiased result (bias ratio = 1). The effects of this adjustment on regional bias are shown in Fig. 2.5. In the mean ROI bias ratios, a substantial reduction in the bias range from ±13% to ±7% was found, accounting for nearly 50% of the original biases. This result shows that by using the information from the refRR-IRR groups, the causes of bias are better understood and explained. The regional biases were also drawn closer to 1, showing that this method can also improve upon the current GPROF biases. Adding the rain profile slope to this adjustment, however, yielded nearly the same results as refRR-IRR alone (not shown), suggesting that this parameter does not meaningfully contribute to explaining the original biases. This is likely related to the similar low-level moisture environments between the regions, which may show random variations in RRslope but not the systematic differences required to explain bias.

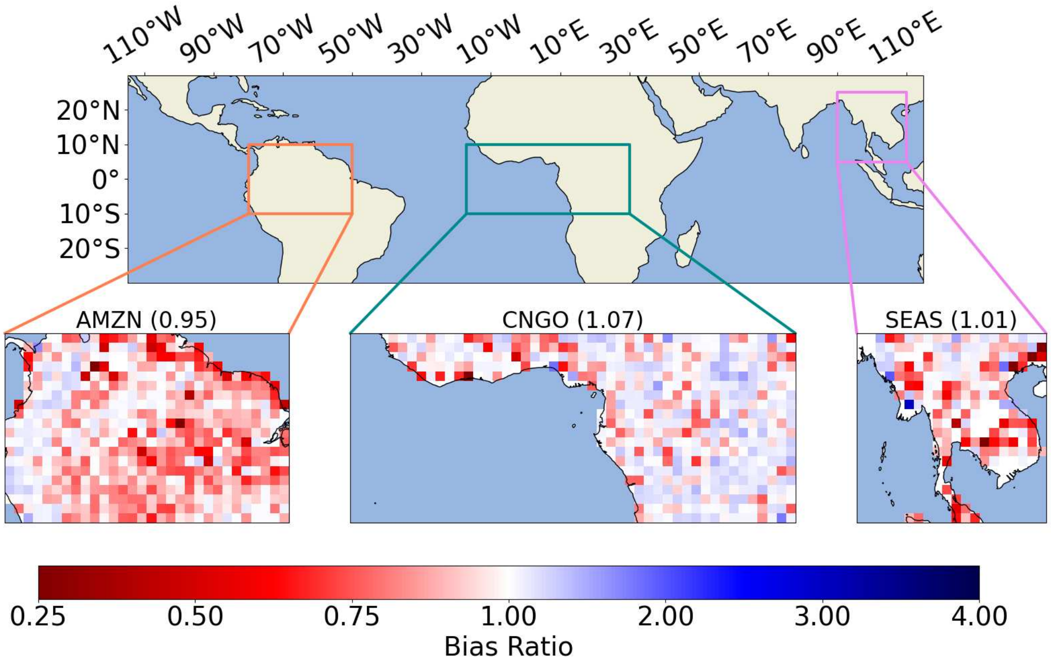

Fig. 2.5. Same as Fig. 2.1, but after refRR-IRR adjustment.

While the mean regional biases showed considerable improvement, Fig. 2.5 also showed that the spatial bias characteristics by region mirrored those shown in Fig. 2.1, with the Amazon remaining categorically underestimated and both the Congo and Southeast Asia overestimated. In AMZN, categorical underestimations over the rainforest and along its northeastern coastline alongside overestimations associated with the Andes which were muted but still present. CNGO remained systematically overestimated, though more prominent underestimation tendencies were noted in areas associated with ITCZ convection and westerly tropical Atlantic flow. SEAS appeared to have a stronger underestimation in the lowland and coastal areas while maintaining, if slightly reducing, the overestimation in the northern mountainous areas. This result indicates that the refRR-IRR adjustment was not enough to fully interpret the systematic bias difference in these regions and other potential explanatory factors remain.

2.3.3. Second-Order Factors

Roughly 50% of the original GPROF bias can be explained using refRR and IRR information, but the systematic regional differences remain. Since these two parameters represent the most likely first-order constraints on bias and the rain profile slope did not contribute additional information, second-order factors were considered. Since the primary information used by GPROF resides in high-frequency channel TBs, 37-GHz TB was examined. This channel is highly affected by surface emissivity but is capable of contributing information regarding both liquid and ice hydrometeors under certain conditions (Toracinta et al. 2002; You et al. 2011). For this study, the polarization-corrected 37-GHz TB (PCT37) was used to mitigate the effects of surface contamination. This quantity was calculated following Cecil and Chronis (2018). Fig. 2.6 shows the bias ratios for select reference rain— IRR groups as a function of PCT37. As shown here, colder PCT37 TBs were generally associated with overestimation and vice versa for warmer PCT37 TBs. This behavior matches the high-frequency channels, where colder TBs are associated with greater ice water paths and represent overestimation. The exact bias representation, however, was strongly affected by the refRR-IRR group being considered. For example, a PCT37 TB of 265 K could have a bias ratio of 1.5 in the high IRR and refRR group or 4 in the high IRR, moderate refRR group. This dependency, along with the fact that the bias ratio did not show strong sensitivity to PCT37 itself, suggests that this factor complements the information provided by the refRR-IRR groups, maintaining its behavior as a second-order effect.

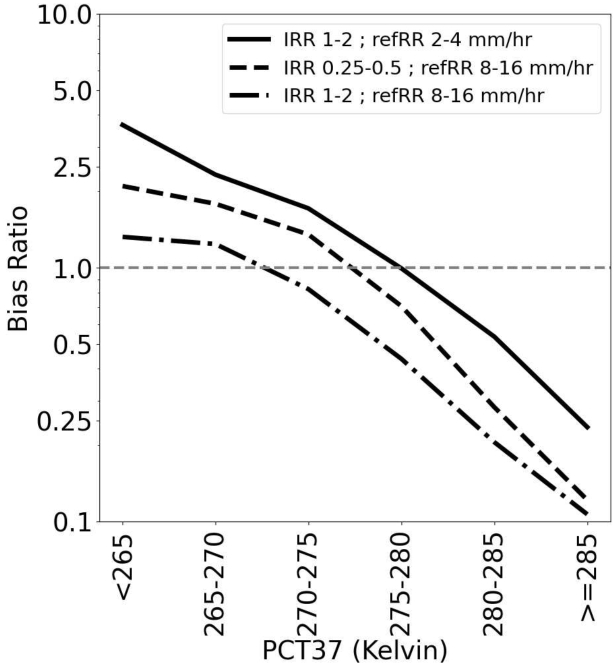

Fig. 2.6. GPROF bias ratios as a function of polarization-corrected 37-GHz TB (PCT37) for three representative refRR-IRR groups.

Given its utility in describing second-order explanatory factors for bias, the polarization-corrected 37-GHz TBs were introduced to the previous bias adjustment analysis. PCT37 was partitioned into six bins defined every 5 K between 265 and 285 K. A new adjustment space was then developed using the combined PCT37, reference rain, and IRR bins. From this space, a new set of bias ratios was developed, and their inverses were used to adjust the GPROF rain rate similar to the refRR-IRR groups. The results of this adjustment are shown in Fig. 2.7. Incorporating this new second-order factor showed further reduction in the range of mean bias ratios by region from ±7% to ±4%, now explaining nearly 70% of the original biases. Regionally, the Amazon and Congo were also drawn even closer to a bias ratio of 1, further indicating an improvement in bias when using this new adjustment method. Southeast Asia, however, shifted from an overestimation to an underestimation tendency, likely due to the higher bias variability in this region. Despite this, SEAS remained comparable to AMZN and CNGO, so the efficacy of this method was believed to be sound.

Looking at the spatial distribution of bias ratio by region in Fig. 2.7, it was apparent that this new adjustment method could better account for the systematic differences in spatial structure noted in both Figs. 2.1 and 2.5. In the Amazon and Congo, the previously observed categorical underestimation and overestimation tendencies were largely removed, and a more heterogeneous mixture of biases remained. Portions of the rainforest within AMZN now display mostly neutral biases and some areas of overestimation, while larger portions of CNGO now show underestimation tendencies where they previously were overestimated. One interesting feature in AMZN was that the Andes had become a source of underestimation. This behavior over mountainous regions also appeared in the mountainous areas in SEAS, suggesting that orography has additional behaviors that are not correctly accounted for in this method. Regardless, this adjustment using the PCT37- refRR-IRR groups yielded considerable improvement for both the range of biases experienced between the regions and better accounted for the systematic differences in the regional spatial structure.

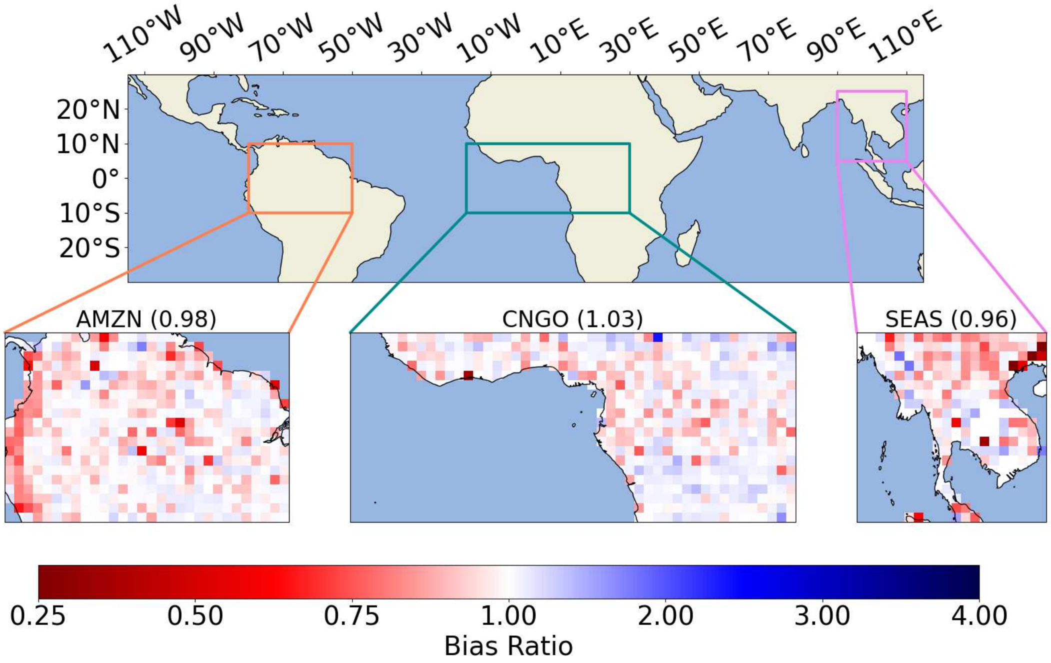

Fig. 2.7. Same as Fig. 2.1, but after the refRR-IRR-PCT37 adjustment.

Despite the apparent benefits of adding the 37-GHz TB information to the previous refRR-IRR adjustments, questions remained as to why this was the case. Since the GPROF algorithm already incorporates the 37-GHz channel as an input, this information was not expected to provide the level of explanation it has shown. Two potential explanations for this behavior exist: PCT37 provides information which is not apparent in the individual 37-GHz channels or the information at 37 GHz is not being utilized properly by GPROF. Analysis of the mean rain and ice water profiles by PCT37 bins and identical bins for each of the 37-GHz channels (not shown) did not show considerable differences in behavior, so GPROF must not be utilizing the 37-GHz information to its fullest. The full picture of this underutilization remains a topic of discovery, but the preliminary analyses performed during this study indicate that the 37-GHz TBs may provide context to the refRR-IRR relationship by reinforcing certain characteristics like ice scattering and introducing newer information regarding the low-level rain water distribution and the depth of the ice layer. In any case, the exact mechanisms by which this parameter can explain bias remain unknown.

2.4 Comparison with GPROF-NN

Having identified refRR, IRR, and polarization-corrected 37-GHz TBs as explanatory factors for regional bias, questions remained regarding the use of these factors in other precipitation retrievals. While refRR and IRR are likely to remain important given the well-established theories behind them, PCT37's utility may be specific to GPROF and thus not applicable elsewhere. To investigate this applicability, an additional retrieval was considered: GPROF-NN, which utilizes a quantile regression neural network (QRNN) approach that has been shown to improve both GPROF's retrieval accuracy and computational efficiency. Further information on GPROF-NN is presented in Pfreundschuh et al. (2022).

To investigate the applicability of these bias constraints for GPROF-NN, the previous bias analyses were reproduced using the 1-D version as the target retrieval, since this version is the more comparable architecture to GPROF. The GPROF-NN dataset used for these analyses was also restricted and scaled using similar methods as for GPROF. It is important to note here that while these steps were taken to match the GPROF-NN data to the GPROF data used previously, some differences between the two retrievals could not be removed. Specifically, the database used for GPROF-NN includes an orography specific adjustment factor and was not restricted to the three regions and two surface types like the study database. These differences, among others, mean that comparing these two retrievals is not exact. Rather, this exercise was designed to investigate if these bias factors produce similar behaviors when used with another algorithm.

GPROF-NN can be shown to have similar biases as GPROF with respect to both reference rain and IRR, so the focus of this comparison is whether adding the 37-GHz information to the refRR-IRR groups provides similar improvements in GPROF-NN as in GPROF. As previously discussed, changes between these groups in the GPROF data reduced the regional bias range from ±7% to ±4%. In the case of GPROF-NN, a similar reduction was found, with some caveats. When considering only the Amazon and Congo, the bias range was reduced from ±3% to ±1%, much like that for GPROF. Southeast Asia, however, was affected heavily by the GPROF-NN's orographic adjustment, resulting in strong overestimation biases remaining present even after data scaling. Changing the scaling method to adjust the two GPROF surface classes separately resulted in very similar improvements as for GPROF in this region, shifting its bias ratio from 1.03 to 0.95. While this change in scaling to compensate for the orographic adjustment complicates the interpretation of these results, these three parameters appear to have comparable explanatory power in GPROF-NN, showing their utility across passive microwave precipitation algorithms.

2.5 Conclusion

Uncertainties in GPROF precipitation originate from multiple sources. Some of these sources are algorithmic, being related to the retrieval technique itself, but the bulk of the uncertainty is related to GPROF's inability to separate TBs which occur under different rainfall conditions. This nonuniqueness is an inevitable cause of uncertainty but can have a more physical connection to large-scale atmospheric properties through the underlying vertical hydrometeor structure. Using bias ratio as an uncertainty quantification metric, several sources of GPROF bias were identified. The first of these sources was refRR, which created biases due to the tendency of GPROF to average multiple precipitation states together when developing its precipitation estimates. This leads to predictable overestimates at low rain rates and underestimates at high rain rates. The second was the IRR, which is directly related to the ice scattering properties at a given location and comprised the primary signal by which GPROF developed its estimates of terrestrial precipitation. In general, increasing IRR results in increasing overestimation due to GPROF's tendency to inflate rain rates in cases of strong ice scattering. The third was polarization-corrected 37-GHz TB, which contextualized the information from the previous factors by identifying multiple second-order differences in the rain and ice hydrometeor structures but was underutilized by GPROF due to its limited information content. A fourth source considered was the rain profile slope, which described the vertical distribution of rain water between the reference level and a near-surface level. Their explanatory power was then investigated by creating data groups through a combination of these parameters and accounting for their respective biases. Using just reference rain and IRR, this resulted in a reduction of the regional bias range from ±13% to ±7%, accounting for about 50% of the original biases. Expanding these groups to include RRslope did not show substantial improvement, but including PCT37 further reduced this range to ±4%. Regarding the spatial distribution of biases within the regions, the refRR-IRR groups did not fully account for the systematic regional differences but adding PCT37 resulted in considerable constraints of these differences.

Since the characteristics of these parameters are physically based and location invariant, the ability of these parameters to explain regional bias must be related to regional differences in their distributions. This can be shown using regional probability distribution functions (PDFs), as shown in Fig. 2.8. In the reference rain PDFs, the Congo appeared to prefer greater rain rates than the other two regions, though the overall distributions were relatively similar. Since the average state of GPROF results in overestimation at low rain rates and underestimation at high rain rates, this behavior suggests an adjustment scenario which would worsen the regional biases if used on its own. This result indicates that refRR should be used more as a constraint on the other factors. In the IRR PDFs, the regional differences were much larger, with the Congo preferring much higher IRRs and both the Amazon and Southeast Asia having broader distributions which also show stronger preferences for lower IRRs. Since high IRRs are typically overestimated and low IRRs underestimated, this factor shows the clearest adjustment criteria for the regional biases. In the 37-GHz distributions, the Congo showed a much stronger preference for lower TBs than the other two regions, with its distribution peaking nearly 5 K lower than AMZN and SEAS. Lower TBs are generally associated with overestimation and high TBs underestimation, so these PDFs present a similar story as those for IRR. For the rain profile slope distributions, the three regions were virtually indistinguishable from each other, causing its inability to provide additional information for bias. It is possible, however, that including regions with substantially different climatologies, such as desert regions, may show a more distinct separation in the RRslope distributions. As such, the utility of these parameters outside of these three regions should also be considered.

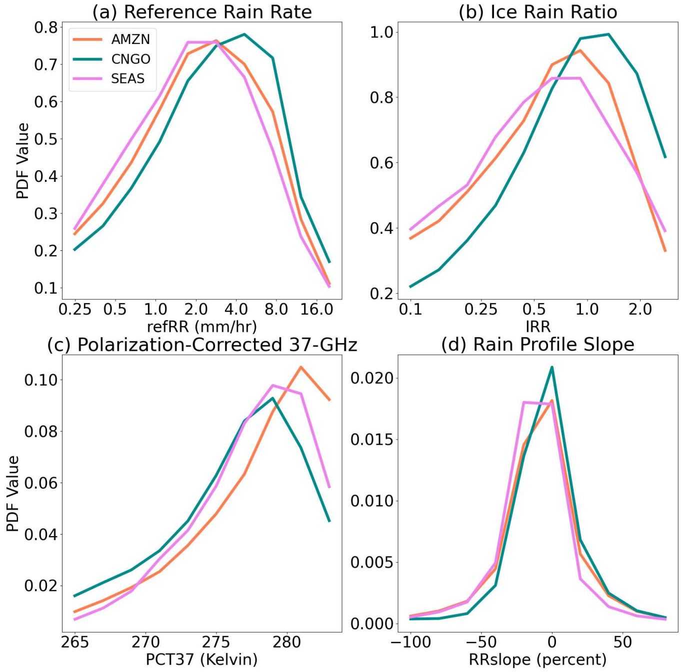

Fig. 2.8. PDFs for (a) refRR, (b) IRR, (c) PCT37, and (d) RRslope by ROI.

The applicability of this information to other algorithms was also tested using the 1-D GPROF-NN, which swaps the traditional Bayesian approach of GPROF for a neural network approach. Using these same groups, similar bias behaviors in the GPROF-NN data were observed, though the interpretation was complicated by differences in the databases and assumptions used to inform the two algorithms. Still, this experiment proved useful for both understanding the innate ability of a retrieval algorithm to distinguish between similar precipitation profiles based on TBs alone and if information about the underlying hydrometeor structure can aid this distinction.

While identifying these explanatory factors for bias is a crucial step forward in retrieval uncertainty quantification, limits to their application remain. The most obvious of these limitations is that both refRR and IRR are radar-derived parameters and thus restricted to the DPR swath. As such, these bias constraints cannot be developed for much of the actual GPROF algorithm, nor can they be used on retrievals from before spaceborne radars existed. The biggest impediment to this is likely IRR, since refRR can be estimated from GPROF rain rate and 37-GHz information is generally available. This parameter may have to be determined using large-scale atmospheric properties, regional climatologies, or some combination thereof. Further work should also include ground observations, as these data would represent a more reliable ground truth than GPM Combined.

The limited scope of this study also presents potential generalization issues. Since these results represent tropical land, there is no guarantee that the same results exist in other climatologically different regions such as the Southwest United States or the Siberian tundra. Moreover, additional parameters not used in this study may be more impactful in assessing bias across climate types and therefore should be included. To this end, the expansion of this study into other, climatologically different locations would provide further information for developing a routine which can be applied globally.

Regardless of these limitations, this study presents a step toward explaining biases in satellite precipitation retrievals through physical arguments. By identifying physically based factors, these biases can be interpreted through the lens of physics as opposed to statistics, aiding in the stabilization of precipitation climate records and adding information to a forecaster's toolbox. In all, this study shows that biases can be understood using known atmospheric processes, presenting an avenue for creating fully interpretable retrieval uncertainties.

CHAPTER 3: IDENTIFYING AND CONSTRAINING ICE EFFECTS ON SATELLITE PRECIPITATION BIASES USING REANALYSIS DATA[2]

3.1 Introduction

Passive microwave satellite precipitation products are driven by assumptions made to connect the radiative information they measure to the processes governing rainfall. A key assumption, particularly over land which provides little radiometric contrast to rain, is the implied correlation between ice aloft and rainfall, manifesting as a depression in high frequency microwave brightness temperatures (Spencer 1986; Vivekanandan et al 1991). While this signature primarily describes cloud microphysical processes as opposed to precipitation processes, Goldenstern and Kummerow (2024) showed that ice content can provide a substantial amount of information about biases in satellite precipitation products, especially when accounting for error sources related to the retrieval architecture. Given the importance of ice scattering in developing satellite precipitation products and its role in creating biases in said products, it is essential to characterize these effects.

Previous studies have shown that satellite precipitation product errors can be attributed to differences in the structure of the systems they represent. Tan et al. (2022) found that the Goddard Profiling Algorithm (GPROF) provided reliable precipitation estimates for convective systems but exhibited strong biases for nonconvective regimes. Additionally, Ryu et al. (2012) found for the same algorithm in a study over the Korean Peninsula that shallow, warm precipitation systems were frequently underestimated by 50% while convective precipitation is less strongly affected. This also speaks to the differences in ice content between deep convective and shallow stratiform systems, as there are robust ice processes ongoing throughout the life

---

[2] **In Review as:** Goldenstern, E., and C. Kummerow, 2025: Identifying and Constraining Ice Effects on Satellite Precipitation Biases Using Reanalysis Data. J. Hydrometeorology.

cycle of deep convection while shallow stratiform precipitation tends to occur below the freezing level and is devoid of ice. These different precipitation regimes also tend to occur under different large scale forcings. Shallow, stratiform precipitation occurs under suppressed vertical motion and static stability, while robust convection occurs within regions of enhanced vertical motion and instability (Steiner and Smith 1997; Nesbitt et al 2000; Tan et al. 2013). These connections suggest that the large-scale environment can also provide information on ice contents.

While direct observations of ice hydrometeors are difficult to achieve, radars have proven useful in quantifying atmospheric ice contents. Ground-based Doppler radar information has an extensive history in the development of vertical profiles for ice water content and the associated particle size distributions (Sato et al. 2009; Tian et al. 2016). Additionally, spaceborne radars like the Global Precipitation Measurement Mission (GPM) Dual Precipitation Radar (DPR; Hou et al 2014) can profile the atmosphere and identify the liquid and solid hydrometeors present. Both methods, however, remain limited in their spatial and temporal coverages. Ground-based radar analyses are only available in the areas where they are stationed, limiting analyses to a handful of developed nations and areas with little interference from terrain. The DPR, on the other hand, can provide these observations irrespective of land surface heterogeneities and socioeconomic pressures, but remains limited to a narrow swath and only flies on one platform, so it does not consistently coincide with these precipitation products. Both methods also have limited time series, with such data available only back to the mid-2010's. As such, an alternative method which can act as a proxy for ice content where this information is unavailable is desired.

This study aims to identify large scale environmental characteristics which can describe the observed ice content information. By providing such a picture, the conditions which foment or obstruct the formation of ice hydrometeors can be identified and utilized to understand satellite precipitation product biases regardless of the availability of radar information. While several studies have investigated the role of the environment in how precipitation is represented by satellite products (Berg et al. 2006; Petkovic and Kummerow 2017; Hsiao et al. 2024), none have attempted to directly use this information for quantitative assessment and constraint of product biases. In this way, this study represents a step forward in predicting regime-dependent biases for satellite precipitation products which are simpler to interpret and more widely available than traditional methods.

This chapter is structured as follows: Section 3.2 details the data used in this study and how it was processed. Section 3.3 outlines the methods used to approach this hypothesis and the results provided. Section 3.4 concludes with a discussion of the analysis results and limitations.

3.2 Datasets and Processing

3.2.1 The Goddard Profiling Algorithm (GPROF)

The target precipitation product for this study is the Goddard Profiling Algorithm Version 7 (GPROF; NASA 2022). This is the current operational version of GPROF and provides both standalone precipitation estimates for the Global Precipitation Measurement Mission (GPM) satellite constellation and acts as the base product for the Integrated Multi-satellitE Retrievals for GPM (IMERG) algorithm. The focus on GPROF serves only to demonstrate the results to be presented; given its reliance on the common principles of microwave radiative transfer, other equivalent products are expected to exhibit similar behaviors. GPROF is a Bayesian algorithm, utilizing an a-priori database of passive microwave brightness temperatures (TBs), ancillary data and associated precipitation rates to develop precipitation estimates via a weighted similarity calculation. This has allowed GPROF to produce globally unbiased precipitation estimates, though substantial local and regional biases frequently occur (Ryu et al 2012; Petkovic and

Kummerow 2017; Bogerd et al 2023; Pfreundschuh et al 2024). GPROF Version 7 data is accessible from the NASA Precipitation Processing System (PPS; https://pps.gsfc.nasa.gov/).

While GPROF provides global precipitation estimates, this study will be focused on observations taken over the Amazon (AMZN), Congo (CNGO) and Southeast Asia (SEAS), as defined in Fig. 3.1. These regions were chosen due to the known disagreement in GPROF biases in these regions, despite similar precipitation characteristics (Petkovic and Kummerow 2017). To separate the impacts of land surface variability from regional precipitation effects, these data were restricted to GPROF surface classes 3 (maximum vegetation) and 17 (mountain). For the mountain class, the operational terrain adjustment factors were reversed to keep focus on GPROF's innate behaviors. These data were gathered from December 2014 to November 2021, with the shifted calendar year interval chosen to avoid truncating seasons in the time series.

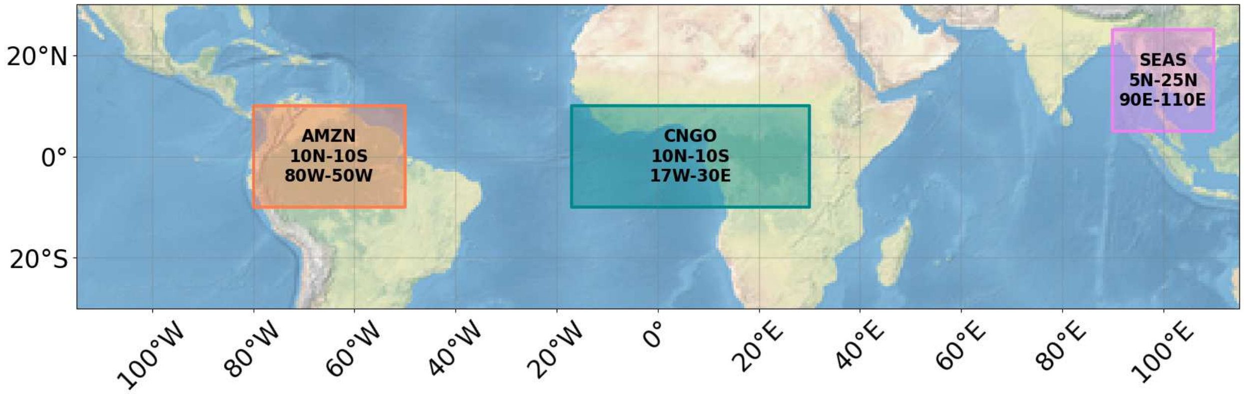

Figure 3.1: The Regions of Interest (ROIs) used in this study. The Amazon (AMZN) is shown in red, the Congo (CNGO) in cyan and Southeast Asia (SEAS) in violet.

3.2.2 The GPM Combined Radar Radiometer Algorithm (CMB)

The radar data utilized in this study is from the GPM Combined Radar-Radiometer Algorithm (CMB; Grecu et al 2016). This algorithm leverages both the GPM Core Observatory's Dual Precipitation Radar (DPR) and Microwave Imager (GMI) to develop physically consistent hydrometeor characteristics and precipitation rates. Though also a retrieval product, CMB relies heavily on radar data and thus is considered a reliable reference for the GPROF precipitation estimates; in fact, this product provides the precipitation rates in the GPROF a-priori database. CMB utilizes spaceborne observations, meaning it can provide information in areas where a more reliable ground truth is unavailable. Due to differences in the swath widths of the DPR and GMI, however, CMB data is only available within the inner third of the GMI swath and not at all for other GPM radiometers, meaning that this data cannot be used to fully diagnose GPROF biases. GPM Combined data is similarly available through the NASA PPS.

The rain and ice water content profiles and near surface precipitation from the GPM Combined algorithm were gathered in the same way as that for GPROF. Further processing of the CMB data was also necessary to ensure proper comparisons with GPROF precipitation. Firstly, since the CMB data is reported at a 5x5km scale while GPROF is reported at 11x18km scale, the CMB data were averaged into the GPROF footprint resolution through an unweighted mean. Additionally, the scan matchups between CMB and GPROF were offset by one scan line to account for the differences in scan geometry between the two products. Finally, the water content profiles were adjusted with a linear growth function for ice water and a linear decay function for rain water respectively to mitigate radar bright banding.

The rain and ice water information from the CMB algorithm were used to derive two parameters: a reference rain rate (refRR) and an ice rain ratio (IRR). This was accomplished by first identifying a reference rain water content (refRWC) and an ice water path (IWP) from CMB water content profiles. From Eq. (3.1), refRWC was determined as the total rain water content (RWC) in a 1km layer centered at 1.5km below the freezing level (FL-2 to FL-1). IWP was calculated as the depth-weighted (dz) sum of ice water content (IWC) from 1.5km above the freezing level to the top of the atmosphere (FL+1.5 to L*), as shown in Eq. (3.2). Since the radar provides these vertical profiles, the determination of the freezing level and layer characteristics can be done directly. The reference rain rate and ice rain ratio were then calculated from these quantities. For refRR, the refRWC was converted to a rain rate through Eq. (3.3), which uses arguments derived from the Marshall-Palmer distribution (Marshall and Palmer 1948). The use of refRR mitigates the impact of near-surface rainfall modification and better captures the precipitative capacity of the systems than the near-surface information from GPM Combined. Additional description of CMB's limitations in assessing near-surface phenomena are include in Grecu et al. (2016). For IRR, the IWP and refRWC were taken in ratio, as shown in Eq. (3.4). Fundamentally, these two parameters represent the individual contributions from precipitation intensity and ice scattering to the biases in satellite precipitation products.

$$refRWC = \sum_{l=FL-2}^{L=FL-1} RWC_l \tag{3.1}$$

$$IWP = \sum_{l=FL+1.5}^{L^*} IWC_l * dz_l \tag{3.2}$$

$$refRR = 17.87 * (refRWC^{1.19}) \tag{3.3}$$

$$IRR = \frac{IWP}{refRWC} \tag{3.4}$$

The biases in this work were defined as the ratio between the accumulated GPROF rain and refRR rain, as shown in Eq. (3.5). While these rain accumulations correspond to different heights above the surface, this comparison is more convenient due to the inability of GPM Combined to assess surface precipitation. Given that this study is focused on tropical environments, which Goldenstern and Kummerow (2024) showed exhibit only slight differences in lower atmospheric rain water content, the differences between refRR and surface precipitation are believed to be minor. The accumulations for both GPROF (RR_{GPROF}) and refRR (RR_{refRR}) can be performed at various spatiotemporal scales depending on the desired analysis. For this study, two scenarios were considered: bulk regional bias, which consists of the total accumulation of rain over the entirety of a given region throughout the full time series, and gridded bias, which accumulates only the rainfall coincident within a given gridbox over the full time series.

$$Bias\ Ratio\ =\ \frac{\sum RR_{GPROF}}{\sum RR_{refRR}} \tag{3.5}$$

3.2.3 The 5th Generation ECMWF Reanalysis Model (ERA5)

The meteorological information for this study comes from the 5th generation of the European Centre for Medium-Range Weather Forecasting (ECMWF) Reanalysis Model (ERA5; Hersbach et al 2020). ERA5 is a globally available weather reanalysis model which provides large scale atmospheric characteristics at relatively fine spatial (0.25 degrees) and temporal (once hourly) resolutions. The model reports many surface-level and atmospheric profile characteristics, allowing for the development of a comprehensive atmospheric parameter dataset for the identification of process-level influences on observation-derived parameters. ERA5 data is available from the Copernicus Climate Data Store (https://cds.climate.copernicus.eu/datasets).

The ERA5 data utilized in this study were matched to the GPROF footprints using nearest neighbors. Additionally, the ERA5 data from three hours prior to the observation time was taken to mitigate the effects of airmass modification known to accompany precipitation. Time lags between 1 - 6 hours prior were investigated when developing this aspect of the data processing and it was found that the 3-hour lag provided an optimal balance between distance from the precipitating environment and proximity to the initiating environment.

3.3 Methods and Results

3.3.1 Ice Content Regime Identification

To understand the regimes which drive the formation of ice in precipitating systems, the ice rain ratio characteristics in this dataset were investigated at seasonal scale over a regular 1.5-degree grid. While other spatial resolutions were tested, 1.5 degrees was chosen to maintain focus on large scale processes which are best resolved by ERA5. Using a seasonal timescale ensures a robust sample size from the GPROF information over this grid, allowing for trustworthy statistical depictions of IRR. These depictions were achieved using probability distribution functions (PDFs) of IRR within the individual gridboxes by season. The data included in these PDFs were restricted to footprints with CMB rain rates between 0.25-32 mm/hr and IRR values between 0-10, which preserves 96% of the accumulated rain in the dataset while mitigating the influence of outliers. This resulted in a dataset of 2,232 IRR PDFs with 8 IRR bins each. After development, these PDFs were weighted by the number of samples, then log scaled.

These weighted and scaled PDFs were taken as input to a K-Means clustering algorithm to identify the main behaviors of IRR. This algorithm was chosen due to its expansive utility in the literature for determining the main behavioral groups of various atmospheric phenomena. To determine the optimal number of clusters for the algorithm, the "elbow method" (Jollyta et al. 2023), was utilized. This method, though more subjective than others, provides an optimal balance of statistical evaluation, through the sum of squared errors by the number of clusters, and user input, through visual interpretation of where the change in error becomes too marginal to warrant the use of additional clusters. For this study, it was determined that five clusters of ice-rain ratio PDFs optimally separated the input data, represented in Fig. 3.2 as the point after which the slope of the line becomes relatively uniform. This figure also shows the average PDFs associated with each of these clusters. From these cluster PDFs, it is apparent that while all IRR values can exist in each cluster, the clusters themselves show distinct preferences for certain ranges. In Cluster 1, the bulk of the distribution lies below an IRR of 0.25, whereupon the density of points begins to sharply decrease, indicating the preference of this cluster for systems in which little to no ice has formed. Cluster 2 also favors lower IRRs but is displaced towards low to moderate amounts of ice, with its preferred mode existing between 0.1 - 0.5, indicating the ability of these systems to develop small amounts of ice. Cluster 3 shifts this preference further, with its preferred mode existing at IRRs between 0.25 - 1 and exhibiting a stronger tail towards higher ice contents. Here, systems with more impactful ice processes are beginning to occur. Cluster 4 shows a distinct preference for higher IRR values, with a central tendency around 0.5 and an increased tendency toward IRR values greater than 1. As such, this cluster is identifying systems in which more robust ice processes are occurring. Cluster 5 shows the greatest preference for high IRR values, with a central tendency of around 0.75 and the greatest point densities for IRR values above 1. This cluster captures systems where very robust ice processes are dominant.

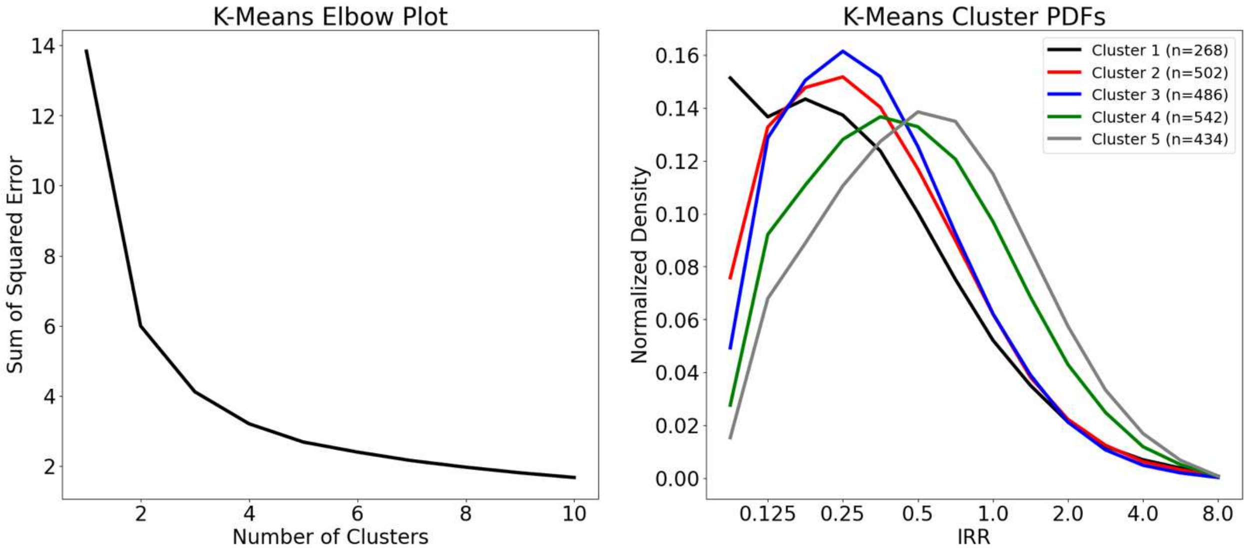

Fig 3.2: The results from the K-Means cluster analysis of the 2,232 IRR PDFs. The leftmost panel shows the results of the elbow method, where after 5 clusters the line slope shows considerable reduction. The rightmost panel shows the average IRR PDF for these clusters, which each colored line representing a different cluster.

While the clusters statistically separate ice-rain ratio, it remains to be seen if they represent distinct precipitation regimes. To this end, an investigation of where these clusters present themselves in space and time was undertaken. To do this, the individual 1.5-degree grids associated with each of these clusters were identified, separated by season, and mapped. The results of this analysis are shown in Fig. 3.3. First and foremost, it is apparent that these clusters show coherent spatial structures, indicating that they describe physical states as opposed to being purely mathematical constructs. These structures also exhibit seasonal variability, suggesting the clusters track the time evolution of these states and further reinforce their physical relevance.

Beginning with Cluster 1, the bulk of the signal resides along the coastlines of these regions, with high densities in the northeast Amazon and coastal Southeast Asia regions during DJF, which are these regions' dry season and non-monsoon season respectively, and sporadic instances across the Congo's equatorial coast both in DJF and JJA. Over AMZN, this is related to the southward shift of the Intertropical Convergence Zone (ITCZ), leaving the subtropical high to suppress vertical growth and sea breeze circulations driven by the trade winds to dominate moisture transport (Gimeno et al. 2012). Over CNGO, the wintertime position of the ITCZ is likely the source of this signal, while in summer its northward movement results in the northerly winds from the Gulf of Guinea becoming the main source of moisture (Davis et al. 2013). For SEAS, the coastal nature of the signal and the timing during boreal winter suggests influences from the region's secondary winter monsoon which force weaker, orographic rainfall systems (Nguyen-Le et al. 2015). Suppressed vertical growth and large-scale oceanic moisture transport favors the development of shallow precipitating systems which remain below the freezing level and therefore do not develop much ice. As such, this cluster encompasses shallow warm precipitation.

For Cluster 2, signals appear in the Amazon in all seasons, with MAM and SON primarily existing along the coastal areas while DJF and JJA show greater presence in the region's interior. The coastal features in the transition seasons align with the development of coastal squall lines, which are known to propagate inland and aid in the development of convection (Alcantara et al. 2011). The Congo sees some instances of this cluster in JJA and, during which time the West African Monsoon is developing (Lebel et al. 2003; Gu and Adler 2004), as well as in SON and DJF which may be related to either the monsoon or the ITCZ position. In Southeast Asia, this cluster tends to occur near topography and is present in all seasons. It is not clear what characteristics this is speaking to, though it may represent a transition between the sea breeze dominant regime to one more influenced by the monsoon. In general, this cluster seems to indicate systems with more substantial vertical growth but still marginal ice formation.

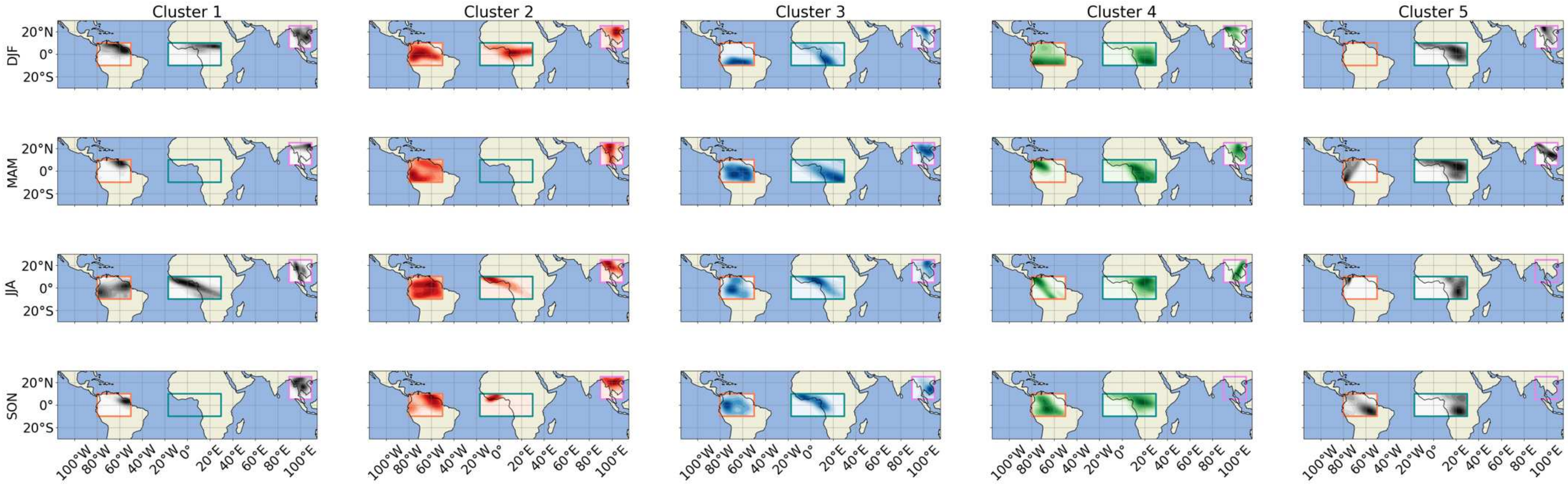

Fig 3.3: IRR Regime Spatiotemporal Characteristics. Each row indicates a different season, and each column is a different cluster. The panel colors correspond with the cluster colors in Fig. 3.2. Darker colors indicate a higher density of points for a given region.

The structures in Cluster 3 appear to be most strongly related to each regions' monsoons. In AMZN, this cluster aggregates in the southern portion of the region during DJF and shifts to a weaker, more northern aggregation during JJA. The transition seasons cover the region's interior, with MAM being the most expansive signal overall. This structural precession broadly follows that of the South American Monsoon, where precipitating systems tend to aggregate near west-central Brazil in boreal winter and transition into the northern portion of the region through boreal summer (Raia and Cavalcanti 2008). Over CNGO, the cluster signal remains focused along the West African coast, with a particularly strong signals during JJA and SON. This timing coincides with the developing and active phases of the West African Monsoon, which aids in the development of convection in these coastal regions through the positioning of the ITCZ and the advance and retreat of the humidity gradient along coastal Africa. The MAM signal in CNGO, however, is largely an inland feature, which complicates this interpretation. For SEAS, this cluster appears frequently from MAM to SON, where it first progresses inland and then retreats. This behavior emulates the lifecycle of the Southeast Asian Monsoon, which first develops in May, reaches its peak during July and August, and retreats to the Maritime Continent during September and October (Lau and Yang 1997). These circulations tend to drive the development of deeper, more organized convection, though their maritime origins lead to less robust ice processes than their continentally driven counterparts and therefore lower ice contents.

For Cluster 4, the signal is preferentially located the regions' interiors. In AMZN, the most comprehensive signal occurs in SON, where the development of mesoscale convective systems (MCSs) under prevailing westerly wind flow characterizes the precipitating systems (Rehbein et al. 2019), while in MAM and JJA the orientation of the signal along the leeward side of the Andes suggests some topographic influence on the developing systems. In CNGO, the signal progresses from south to north by season, following the progression of the African Easterly Jet (Zipser et al. 2006; Nicholson et al. 2022). Over SEAS, this cluster again shows considerable seasonal variability, though its situation generally near topographic features within the interior of the region indicates the potential for orographically-forced convection. These depictions seem to indicate that this cluster is primarily capturing convection which is highly associated with complex topography.

Cluster 5 is most apparent in the interior of the Congo and exhibits little seasonality. This region is known as one of the most convectively active places in the world, where deep vigorous convection develops through energy transport by the African Easterly Jet and interactions with the Ethiopian Highland and Darfur Mountain range. Additional occurrences of this cluster in the Amazon and Southeast Asia tend to occur near regions of complex topography, which can enhance convective growth through upslope flows. Particularly in AMZN, this cluster occurs in an area with enhanced lightning activity during MAM, potentially resulting from the deeper penetration of the trade winds into the continent and interacting with the Andes. As such, this cluster describes a regime which favors the development of deep convection known for robust ice production.

3.3.2 Large-Scale Environmental Interpretation of Regimes

Having identified these five ice rain ratio regimes and many of the large-scale processes associated with them, a more physical description of these states was pursued using ERA5 information. To simplify the analysis, three ERA5 variables were considered: Convective Available Potential Energy (CAPE), Total Column Water Vapor (TCWV) and Column Average Temperature (Tavg). CAPE represents the potential of developing convection, which both speaks to the energetics of the system and the potential to form enhanced ice contents. TCWV was chosen due to its representation of the bulk moisture characteristics present, which presents a limit on the amount of ice that can form and may speak in part to the separation of maritime and continental airmasses. While Tavg is a relatively simplistic description of the atmospheric temperature profile, this parameter was chosen over other parameters such as the vertical temperature gradient due to its more straightforward relationship with atmospheric depth. Higher column average temperatures indicate deeper atmospheric columns, which can allow for greater vertical development of precipitating systems and therefore allow them to produce greater amounts of ice. It is worth noting that Tavg is a derived quantity, represented in Eq. (3.6) as the unweighted mean value of a given ERA5 temperature profile between 1000 and 100 hPa (L=27 layers).

$$Tavg = \frac{1}{L}\sum_{l=1}^{L} T_l \tag{3.6}$$

Having identified these variables, their characteristics were then compared between the identified IRR regimes and shown in Fig. 3.4. From these parameters, several observations can be made regarding the relationships between the ERA5 parameters and the IRR regime clusters. Firstly, the medians and interquartile ranges (IQRs) of CAPE and Tavg show a roughly linear increase with the IRR clusters, indicating that as the available energy and temperature increases, greater ice formation occurs. Given the ability of CAPE to distinguish environments more likely to produce convection from those associated with stratiform systems, this corresponds with the types of precipitating systems separated by the cluster regimes. The relation of Tavg to the depth of the atmospheric column also suggests that systems which produce greater amounts of ice tend to be deeper than those which produce little ice, again following the regime identification of shallow and deep systems. Unlike CAPE and Tavg, however, TCWV does not show an immediately identifiable relationship with the IRR clusters. The behavior of this parameter with the clusters appears double valued, as the IQRs between the clusters overlap significantly. In the median values, however, Clusters 1 through 3 generally show both enhanced TCWV amounts and a general increase by cluster. For Clusters 4 and 5, however, the median values noticeably drop and show a slight decrease by cluster. Given the cluster characteristics discussed previously, it is possible that TCWV is separating moist maritime airmasses from comparatively drier continental airmasses, though this analysis does not provide enough information to definitively make this determination. Though these data do not directly account for any seasonal variations, additional analyses which did consider this for TCWV and Tavg had very similar traits (not shown), indicating that the seasonal cycle does not strongly affect these results.

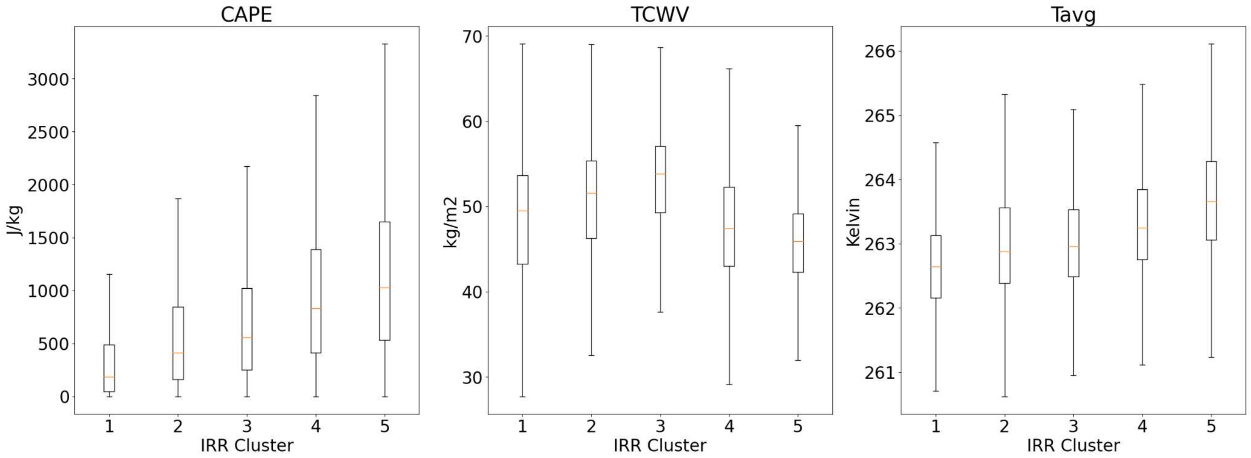

Fig 3.4: ERA5 parameter distributions by ice-rain ratio cluster for (left) CAPE, (center) TCWV and (right) Tavg. The boxes represent the interquartile range of each variable by cluster, while the whiskers extend to the 10th and 90th percentiles.

To investigate the use of CAPE, TCWV and Tavg as proxies for the ice rain ratio regimes, these parameters were used to recreate the K-Means analysis. To do this, the median values for each variable were determined for each regime per Fig. 3.4. These medians were then compared with the individual ERA5 values in the dataset through Euclidean distance. The median which minimizes this distance is then assigned as that observation's regime. These reconstructions were then mapped and the spatiotemporal characteristics compared with the original clusters, as shown in Fig. 3.5. For illustrative purposes, only Cluster 1 is shown here, though similar qualities were found for the remaining clusters.

Looking first at the CAPE estimated regime, there is a high degree of correspondence between the reconstructed and original cluster. The strong coastal signals in the Amazon and Southeast Asia during DJF, JJA and SON are present, as well as the ITCZ shifting behavior found over the Congo. Areas where the CAPE estimation deviates from the original regime include the Andes Mountains and the mountainous regions of Southeast Asia, where the reconstruction shows a persistent signal with little seasonal variation. This behavior may result from an artifact in the CAPE calculation. Since CAPE is a vertical integral through the atmosphere, if part of the column is missing due to being below the terrain elevation, the integration would return a lower value. Other discrepancies between the CAPE cluster and original cluster are spurious, indicating that CAPE does well at recreating this regime.

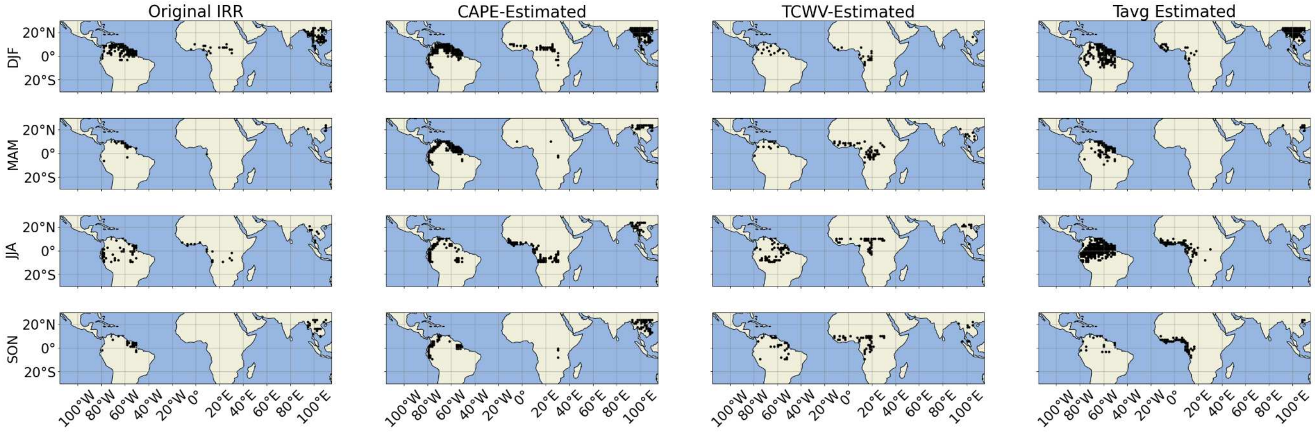

Fig 3.5: Comparison of Cluster 1 spatiotemporal characteristics between the (leftmost) K-Means, (center left) CAPE, (center right) TCWV and (rightmost) Tavg methods. The rows again represent the individual seasons.

Moving to TCWV, the reconstruction does a poor job of emulating the original regime. The signals in the Amazon are largely absent, though the MAM and JJA recreations are somewhat comparable. The behaviors in the Congo are poorly represented, with considerable erroneous attributions in all seasons. Much of this erroneous signal is in the Sahel, which may impact the reconstruction due to its more arid nature. In Southeast Asia, the cluster signals are again absent. This poor performance should come as no surprise given the apparent lack of a relationship between TCWV and the original clusters, though it is unclear why this is so. In any case, these results show that TCWV alone cannot reconstruct these regimes.

For the Tavg reconstruction, there is considerable overextension of the cluster, particular over the Amazon. This is most apparent in DJF and JJA, there large portions of the interior AMZN are erroneously included in the cluster reconstruction. During MAM and, to a lesser extent SON, the AMZN cluster characteristics are reasonable recreated. Over the Congo, the coastal elements during JJA are well represented, though the remaining seasons are less so, with SON containing an erroneous signal along the coast. The behaviors over Southeast Asia show many similarities with the CAPE reconstruction, though it does seem to do better in MAM and worse in JJA and SON. One plausible reason for these discrepancies could come from the homogeneity of the temperature characteristics in these regions, as the natural variability of the system may blend adjacent regimes together. Nonetheless, Tavg shows some skill in reconstructing these regimes.

These parameters can also be combined into a multivariate system to identify the IRR regimes. This was done my expanding the Euclidean distance calculation to include CAPE, TCWV and Tavg together, along with incorporated weights for each variable, as shown in Eq. (3.7). Here, C_{MDN}, W_{MDN} and T_{MDN} are the median values of CAPE, TCWV and Tavg for a given cluster and $w_C = 0.4$, $w_W = 0.2$ and $w_T = 0.4$ are the weights assigned to those respective parameters. These weights were determined manually based on the subjective interpretation of each parameter's ability to correctly identify the IRR clusters and the observed effects on the multivariate system's performance. Further work with this system should reconsider these weights to identify their optimal values in a more robust manner.

$$Dist = \sqrt{w_C(CAPE - C_{MDN})^2 + w_W(TCWV - W_{MDN})^2 + w_T(Tavg - T_{MDN})^2} \qquad (3.7)$$

Fig. 3.6 shows the confusion matrix for this method. If the reconstruction is perfect, this matrix would be diagonal. From this figure, the use of the ERA5 information in this manner shows promise in attributing these clusters. The general behavior of the matrix is diagonal, indicating that this method is moderately skilled at identifying these IRR regimes. Clusters 1 and 5 are particularly well recreated, with 61% and 74% of the regime instances correctly identified. Clusters 3 and 4 are reasonably well attributed at 45% and 41% respectively, which is the majority-case identification for these clusters. Cluster 2 performs the worst in this method, with only 22% of its attributions being correct. The misattributions for this cluster, however, are predominantly in Clusters 1 and 3, which indicates that this method is not misattributing this cluster to wholly unrelated ones like Cluster 5. In all, this method shows reasonable skill in identifying the IRR clusters, though it needs further work to improve these attributions.

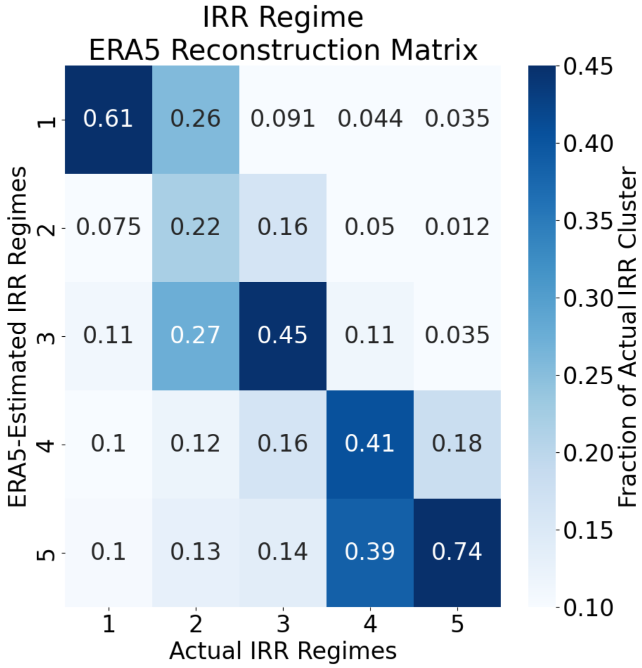

Fig 3.6: Confusion matrix for ERA5-reconstructed clusters.

3.3.3 Precipitation Bias Adjustment Using ERA5

With a reasonably skilled reconstruction of the identified ice-rain ratio regimes using ERA5 now developed, an investigation of how this information impacts GPROF precipitation bias was undertaken. First, the original bias characteristics of the regions of interest were identified, as shown in Fig. 3.7. From this figure, it is apparent that these regions show little consistency in their biases. The Amazon is categorically underestimated, with a bulk bias ratio of 0.93 and widespread gridded bias ratios below 1. The one exception is an overestimation of rainfall on the windward side of the Andes Mountains, which may be related to the GPROF orographic adjustments. The Congo, on the other hand, experiences categorical overestimation, with a bulk bias ratio of 1.07 and gridded bias ratios generally exceeding 1. Some areas of note are found along the West African coast, where the gridded biases indicate underestimation, potentially related to the impacts of precipitating systems with weaker ice signatures that occur during onshore flow regimes. Southeast Asia experiences considerable overestimation, with a bulk bias of 1.10, though the gridded biases show a large degree of heterogeneity. Areas of elevated terrain are preferentially overestimated, while the lowland and coastal regions are underestimated. In all, these regional characteristics amount to a bias range of ±10 points, emphasizing the large discrepancies in performance between these regions.

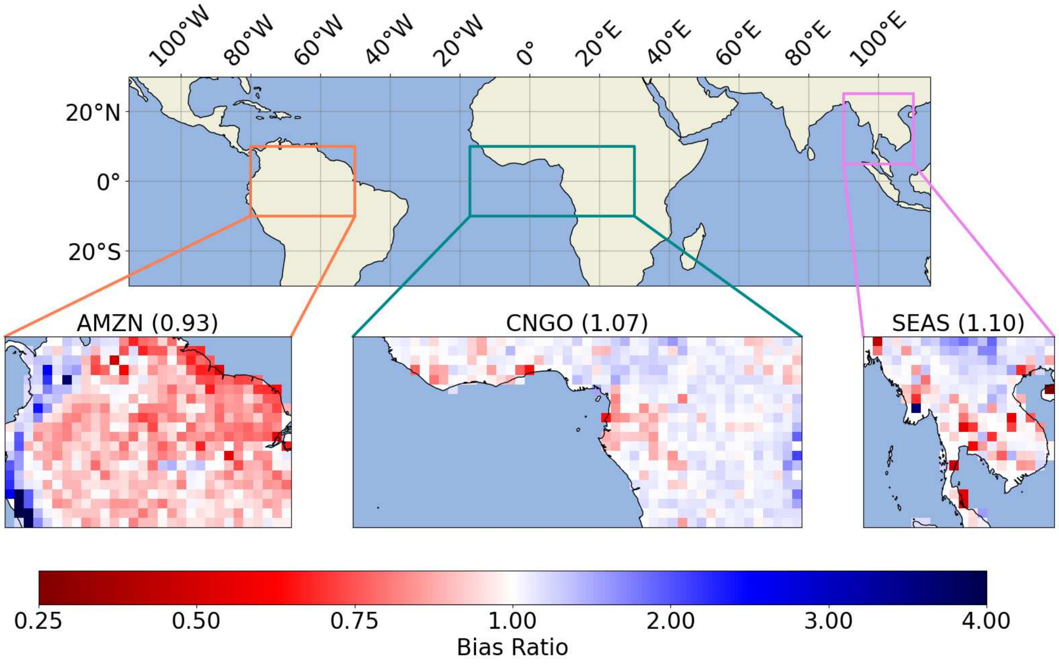

Fig 3.7: The bulk (parentheses) and gridded (map) biases for the regions of interest. These biases were calculated using Eq. 3.5, with refRR as the truth precipitation.

Following this analysis, the impact of ice content on regional bias was investigated. This was done by utilizing the methodology from Goldenstern and Kummerow (2024) where suspected predictors were grouped and the residual bias identified by removing the contributions to the total bias by each group. For this study, the ice rain ratio regimes served as the ice content groups. The results of this adjustment are shown in Fig. 3.8. Over the Amazon and Congo, considerable improvements in the bulk biases are noted, with AMZN going from 0.93 to 0.98 and CNGO from 1.07 to 1.00. This results in a reduction in the bias range between these two regions from ±7 points to ±2 points, or a 70% improvement in the regional bias consistency. The gridded biases also show considerable improvements. In AMZN, the magnitude of underestimation is noticeably decreased, though the overestimation in the Andes region persists. In CNGO, the interior of the region has shifted to a modest underestimation tendency, while the underestimation previously observed along the West African coast persists. Over Southeast Asia, the bulk bias characteristics are worse than without adjustment, going from 1.10 to 1.16. This is largely tied to the areas of elevated terrain in the northern portion of the region, where the previous overestimation tendencies appear to have been enhanced by the adjustment. These areas are traditionally difficult for satellite precipitation products, which may be contributing to this degraded performance. Still, these behaviors in the bulk and gridded bias characteristics by region show the IRR regimes represent a considerable constraint on GPROF biases.

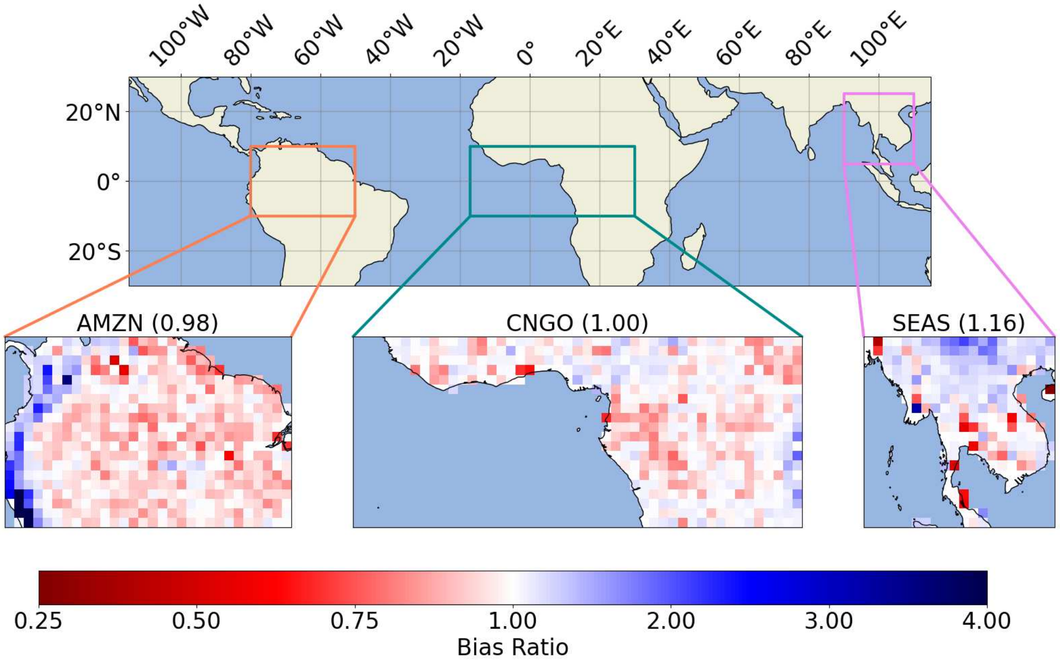

Fig 3.8: The same as Fig. 7, but for the residual biases remaining after accounting for contributions from the ice-rain ratio regimes.

Finally, the previous constraint analysis was redone using the ERA5 reconstructed regimes in place of the ice-rain ratio regimes, with the results shown in Fig. 3.9. Comparing these results with those from Fig. 3.8, it is apparent that the ERA5 reconstruction reproduces the observed constraints on GPROF bias. In the bulk biases, the Amazon and Congo remain within the ±2 point range determined by the IRR regime adjustment, though the Congo now has a slightly higher overestimation tendency. In the gridded bias characteristics, both regions appear very similar structurally to the IRR regime adjustment. AMZN represents modest underestimation with the Andes being overestimated, though there is enhanced underestimation along the northeastern coast. CNGO's biases show little structural differences between the two adjustments, with the most notable difference being a slightly higher overestimation tendency in the northern portion of the region. Interestingly, Southeast Asia is now better constrained than with the IRR regimes, with a bulk bias of 1.05 and noticeably reduced overestimation tendencies in the gridded biases. This appears to be driven by a substantial reduction in the overestimation over the elevated terrain, though the exact cause is unclear. Nevertheless, these results show that the large-scale environment can be used in lieu of the ice content information and be expected to perform similarly when addressing regional biases.

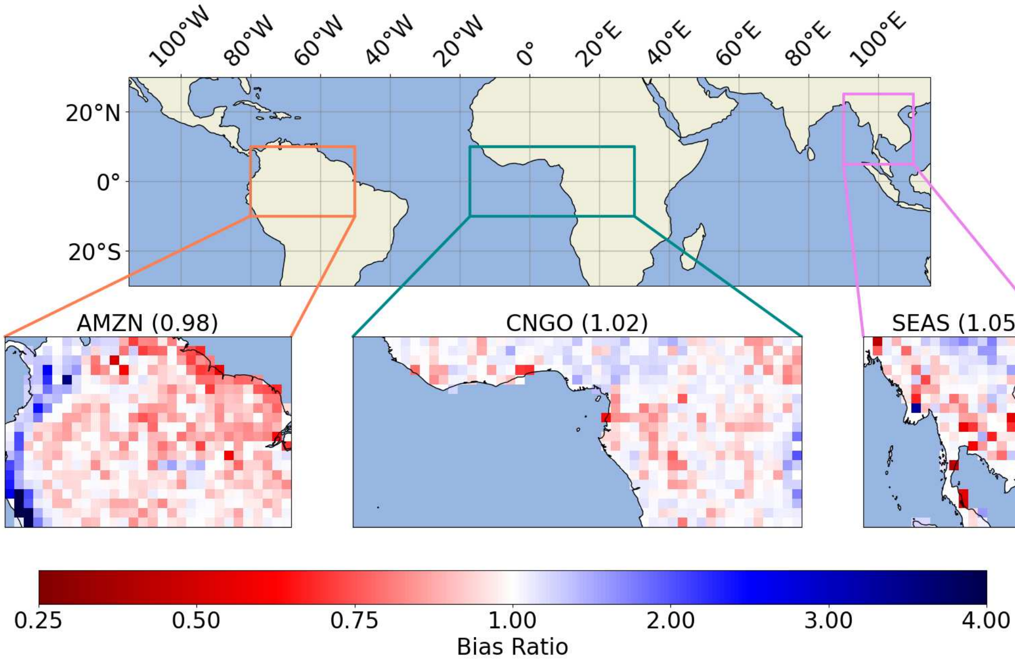

Fig 3.9: The same as Fig. 3.8 but for the residual biases remaining after accounting for contributions from the ERA5 reconstructed clusters.

To investigate the ability for these results to generalize to other time series, an additional test was performed using the portion of the dataset from December 2020 to November 2021. These data were separated and treated as an insulated time series, which were then assigned to an ice-rain ratio regime and adjusted similarly as the full dataset using the ERA5 clusters. The results of this analysis are shown in Fig. 3.10. Comparing these results with those from Figure 3.9, there is considerable consistency between the two. The bulk biases are comparable, with the Amazon being 0.98 and 0.96, the Congo being 1.02 and 1.05 and Southeast Asia being 1.05 and 1.08 for the full and insulated time series, respectively. The gridded biases also show very consistent structures, though the greater noise in the insulated time series is contributing to greater bias magnitudes. In AMZN, the overestimation near the Andes remains, as do the overestimation characteristics of the elevated terrain in SEAS. Over CNGO, the bias structure is also quite similar, but with broader extent and more intense underestimation, especially near the west-central African coast. Though the exact intensities differ, the similarities presented indicate that the results from the full dataset can generalize beyond their original time series.

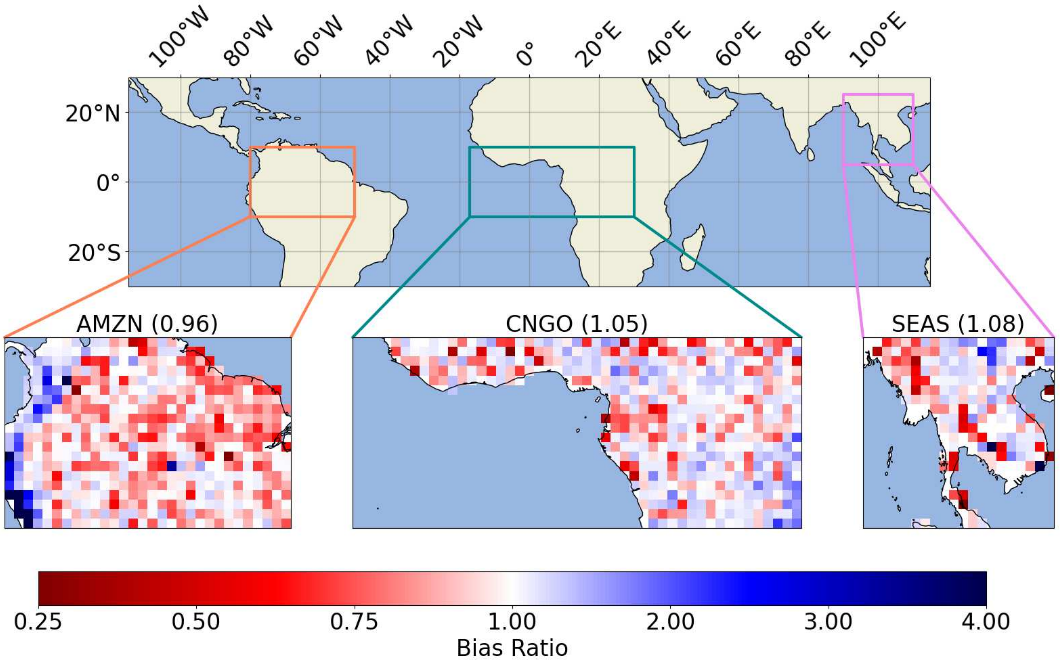

Fig 3.10: The same as Fig. 3.9 but using information from Dec 2020 - Nov 2021 only.

3.4 Discussion and Conclusions

Tropical precipitating systems exist in several regimes which can be discussed in terms of their ice contents. The regimes identified in this study are sensitive to the environment in which they reside and can be described in terms of their depth, convective capacity, and the moisture characteristics of the originating airmass. The first regime is shallow nonconvective maritime precipitation, characterized primarily by coastal circulations and sea breeze effects. The second regime is modest depth, weakly convective maritime precipitation, driven by coastal squall line formation. The third regime is moderately deep, convectively active, mixed maritime-continental precipitation, where monsoonal circulations force deeper but still ocean-influenced convective systems. The fourth regime is moderately deep, convectively active continental precipitation, where continental airmass characteristics and stronger orographic influences allow for much higher contributions of mixed-phase and ice processes in rainfall development. The fifth regime is very deep, convectively active continental precipitation, in which the most vigorous convective systems with the greatest ice contents reside. These regimes exhibit spatiotemporal characteristics which attribute them to these well-known atmospheric processes, indicating that the environment can diagnose them. The large-scale environmental characteristics of these ice regimes were found to be explainable using ERA5 CAPE, TCWV and Tavg. Individually, CAPE and Tavg perform reasonably well and TCWV struggles, while in combination these parameters show reasonable skill in identifying the IRR regimes. This translates into similar bias explanatory power as using these regimes, showing that precipitation product errors can be represented using the large-scale environment. Comparisons using insulated subsets of the full dataset also show good correspondence in bulk and gridded bias behaviors, indicating that these results can generalize outside of the original time series.

Despite these promising results, there are multiple limitations which must be addressed. First and foremost is the limited scope of the analyses. By limiting this study to these three tropical land regions, it is not clear how these results function on a global scale. Sensitivity studies in which one of these regions is withheld from the K-means clustering analysis do however indicate some generalizability of this information. Fig. 3.11 shows an example of this for an experiment where Southeast Asia was withheld. From this depiction of Cluster 1, there is almost no difference between the original regimes and those developed without information from SEAS. Experiments withholding the Congo and the Amazon also show similar behaviors, though the comparisons withholding AMZN show greater deviations due to the lack of information only found in this region. These results suggest that while the regional sensitivity of these regimes is minimal, there do exist scenarios in which a regime which had not been previously encountered can noticeably affect this process. Further work might consider the utility of developing these clusters in a single region (i.e. AMZN only) to further evaluate the regional generalization, as well as including climatically different regions like those in the midlatitudes.

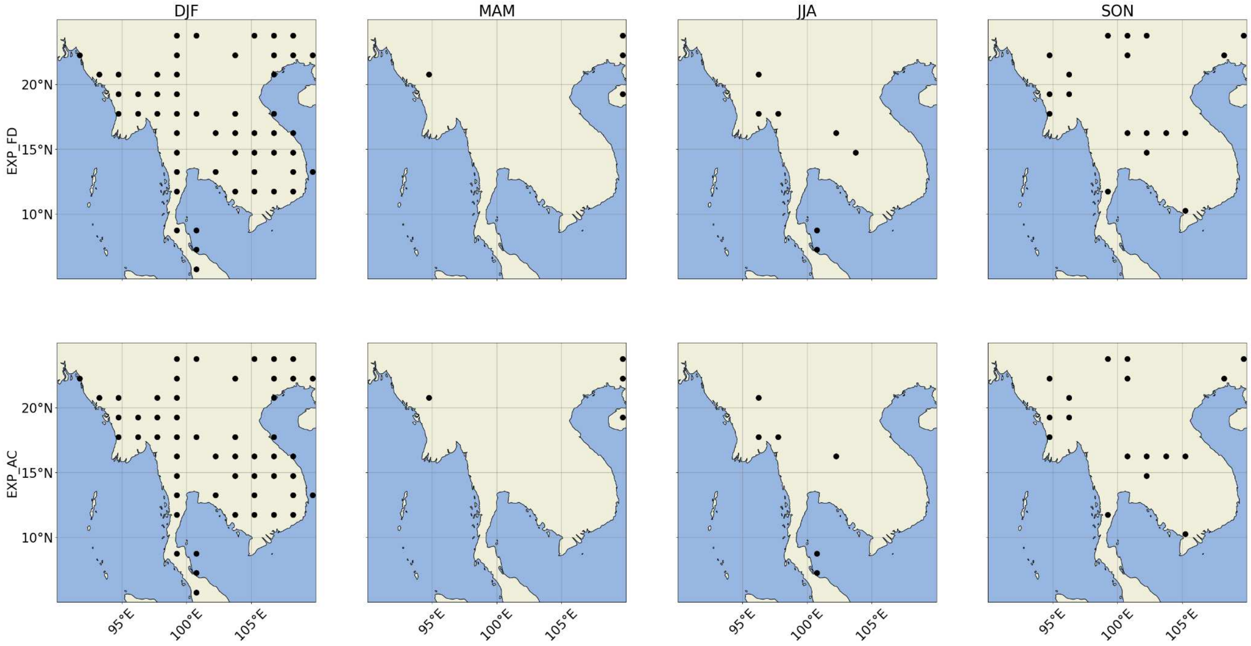

Fig 3.11: The regional distribution of Cluster 1 for Southeast Asia. The black dots show locations where the cluster was identified. The top row is the original dataset, which includes information from SEAS while the bottom row uses only the information from AMZN and CNGO to identify the SEAS points. Each column represents a season.

Also, it is well known that satellite precipitation biases are highly dependent on rain rate, which is not investigated here. This could potentially influence the bias characteristics found in each of the IRR regimes, as a given IRR value can be associated with many different rain rates. Fig. 3.12 shows this effect, with the bias ratio for a given IRR value generally decreasing in magnitude with increasing rain rate. While this figure shown very large differences in the bias ratio as a function of rain rate, it is also worth noting that for rain rates between 1 – 4 mm/hr, which encompass the bulk (about 66%) of the accumulated rain in the dataset, this dependency is much weaker than outside this range. This would suggest that while the rain rate does affect bias, this is a secondary effect to ice rain ratio, and therefore the ERA5 environment, where the precipitation is most impactful. As such, the results shown here are expected to be representative of the full effect on GPROF biases, though further studies should also include the rain rate dependency especially when considering more extreme precipitation events.

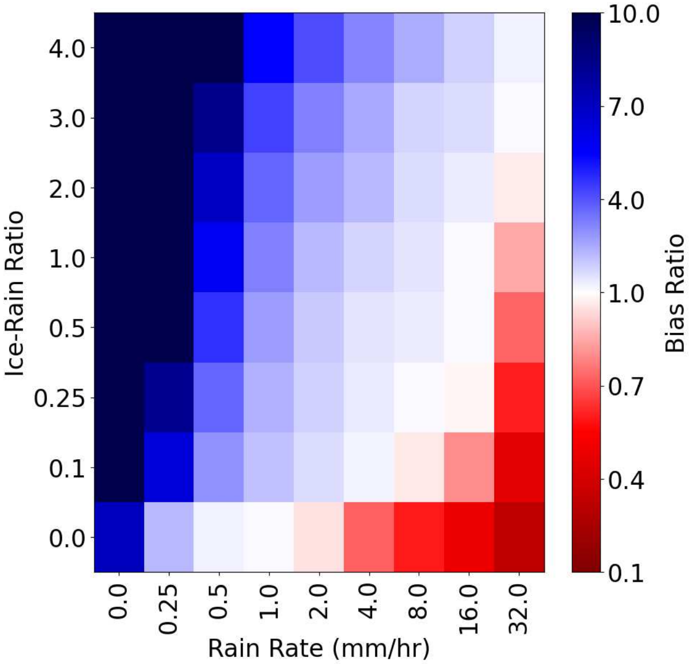

Fig. 3.12: The average bias ratio by groups of ice-rain ratio and rain rate. Red colors show underestimation while blue colors represent overestimation.

Additional limitations include the incomplete descriptions of the large-scale environment associated with these regimes and the spatiotemporal resolution at which they were evaluated. The use of CAPE, TCWV and Tavg only does not constitute a comprehensive picture of the large-scale state and should be expanded on in future work. Specifically, kinematic forcings like vertical velocity, mass convergence and relative vorticity have been shown to impact the precipitative capacity of tropical convective systems and thus may better delineate the IRR regimes. Also, the use of temperature and humidity profile information as opposed to column-integrated values may provide greater insights. These additional parameters could be incorporated directly into the cluster attribution method outlined in this study, potentially improving its ability to identify the individual clusters. The use of a 1.5-degree seasonal scale analysis to understand instantaneous bias characteristics is also a complication due to the considerable amount of smoothing from the "coarseness" of the aggregation. Precipitation formation is strongly influence by small-scale, fast-varying dynamics which this method cannot capture. This is largely a limitation of the datasets used, as the GPROF and ERA5 native resolutions are too coarse to resolve these processes. Despite this, preliminary analyses at finer spatiotemporal resolutions (i.e. 0.5-degree weekly) show comparable performance, so it is believed that the lessons learned during this study can be translated to finer timescales and should be pursued in future studies.

This study shows that if the large-scale environment can be adequately characterized, information on radar-derived quantities such as ice content can be diagnosed and utilized to explain satellite precipitation product biases. This represents a step forward in creating interpretable and global precipitation bias information using domain knowledge of atmospheric processes in cases where direct assessments are not possible due to a lack of coverage spatially or temporally. With further advancements on this topic, it is possible that these methods can be used to validate these products in regions and times previously considered impossible.

CHAPTER 4: PREDICTING PASSIVE MICROWAVE PRECIPITATION BIASES USING METEOROLOGICAL INFORMATION

4.1 Introduction

Precipitation estimates from passive microwave satellite products are integral to our understanding of the global hydrologic cycle due to their ability to provide information in locations which lack comprehensive in-situ measurement capabilities. These products rely on the indirect and complex relationships between the radiative properties of clouds and the precipitation they produce (Spencer 1986; Tapiador et al. 2012; Vivekanandan et al 1991), which results in quantifiable errors. These errors, as well as the precipitation they are associated with, exhibit high variability in both space and time, making their quantification a uniquely challenging task (Krajewski et al. 2003; Tian et al. 2007). Given the importance of satellite precipitation products both for understanding the global hydrologic cycle and as the main source of weather forecasting information for much of the developing world, it is therefore essential to provide a comprehensive and actionable description of these errors.

In recognition of this need, several methods have been developed by which to assess satellite precipitation product errors. The most prominent of these methods is ground validation, in which high-quality reference precipitation data are used to identify product errors (Ebert 2007). Such studies are routinely used in the calibration of satellite precipitation missions (i.e. Petersen et al. 2020) and serve as a gold standard for error quantification. Other error quantification methods use statistical frameworks to broaden their application. The Two-Dimensional Satellite Rainfall Error Model (SREM2D; Hossain and Anagnostou 2006) utilized joint probability distributions of satellite and reference rain rates to stochastically reproduce the error characteristics of the satellite product at multiple spatiotemporal scales. Similarly, the Precipitation Uncertainties for Satellite Hydrology (PUSH; Maggioni et al. 2014) framework, which estimates both categorical error (i.e. hit, miss and false alarm) as well as the probability distribution of actual precipitation at quarter-degree daily resolution. Wright et al. (2017) also attempts to produce a probability distribution of the reference precipitation using a censored shifted gamma distribution (CSGD) to determine errors. Yet another method presented by Adler et al. (2012) circumvents the use of a reference precipitation dataset altogether, instead utilizing an ensemble of products to determine error as the deviation of a single product from the ensemble mean.

While these methods have provided considerable insight into satellite precipitation errors, they are not necessarily capable of providing global precipitation errors. At the core of this problem is the reliance on a reference dataset, which is not universally available. Since systematic errors are known to vary by location and cloud properties, there is a high degree of variability in these statistics. The error information developed in areas which have these reference data therefore cannot be immediately applied elsewhere, preventing their use on a global scale. While the product intercomparison method highlighted by Adler et al. (2012) does circumvent this issue, its reliance on the products themselves results in error assessments which may not be representative of the physical state, but rather the statistics of the ensemble. As such, an alternative method which can provide physically based satellite precipitation errors that can also generalizes to any location is required to accurately assess global errors.

This study aims to develop a method which uses information on the large-scale environment to produce physically based satellite precipitation errors. Previous literature has explored the relationships between meteorological variables related to atmospheric stability, moisture and shear, among others, to both satellite precipitation and its errors (i.e. Berg et al. 2006; Hsiao et al. 2024; Nesbitt et al. 2000; Petkovic and Kummerow 2017; Tan et al. 2022), but none have used this information to directly quantify these errors. Since the formation of clouds and precipitation follows certain rules dictated by these environmental conditions, it stands to reason that using this information should also provide information regarding the error characteristics of these precipitation products. By providing such a method, this work represents a first step towards the development of satellite precipitation product errors which are globally available and interpretable through our knowledge of atmospheric science.

This chapter is structured as follows: section 4.2 described the data utilized in this study as well as its initial processing. Section 4.3 describes the development and evaluation of the bias estimation model, termed the Satellite Precipitation Errors from Ancillary Data (SPREAD) model. Section 4.4 describes the application of SPREAD to out of sample data in the tropics and midlatitudes to further evaluate its performance and investigate its ability to generalize to data it has not encountered previously. Section 4.5 discusses these results and provides some conclusions.

4.2 Datasets and Processing

4.2.1 Satellite Precipitation: GPROF Version 7

The satellite precipitation product used in this study is Version 7 of the Goddard Profiling algorithm (GPROF; NASA 2022). This product was developed for use with passive microwave radiometers in association with both the Tropical Rainfall Measurement Mission (TRMM; Simpson et al. 1996) and the Global Precipitation Measurement Mission (GPM; Hou et al. 2014), providing global precipitation estimate from multiple satellite platforms. Though this study is focused on GPROF, its use of common principles in microwave radiative transfer means similar algorithms should exhibit comparable behaviors. GPROF is a Bayesian algorithm, referencing an a-priori database of brightness temperatures (TBs) and ancillary data with associated precipitation rates to predict the precipitation related to an observed set of TBs through weighted similarity. Such a method allows GPROF to provide robust precipitation information at a global scale. Version 7 of the GPROF algorithm is available through the NASA Precipitation Processing Subsystem (PPS; https://pps.gsfc.nasa.gov/).

4.2.2 Reference Precipitation: CMB and MRMS

The reference precipitation data used in this study comes from two different radar products: the GPM Combined Radar-Radiometer Algorithm (CMB; Grecu et al. 2016) and the Multi Radar Multi Sensor System (MRMS; Zhang et al. 2016). CMB is a satellite retrieval system that utilizes information from the GPM Dual Precipitation Radar (DPR) and Microwave Imager (GMI) in an optimal estimation framework to assess the precipitation and hydrometeor characteristics as observed by the GPM Core Observatory. Though not a direct observation dataset, CMB's reliance on radar data provides it with much greater information content than other satellite products, making it an adequate reference data source. As with GPROF, CMB data is available through the NASA PPS (https://pps.gsfc.nasa.gov/). The Multi Radar Multi Sensor System is a merged product which takes information from multiple sources, including the Next Generation Weather Radar (NEXRAD) system, rain gauges and numerical model data, to produce mosaic radar and precipitation fields. These data products have been used operationally to produce severe weather, aviation and quantitative precipitation forecasting information, and have also been used for ground validation of the GPM data products over the Continental United States (CONUS). These data are accessible through the Iowa State Meteorological Data Archive (https://mtarchive.geol.iastate.edu/).

4.2.3 Large-Scale Meteorological Data: ERA5

The data used to investigate large-scale environmental conditions comes from the fifth generation of the European Centre for Medium Range Weather Forecasting Reanalysis Model (ERA5; Hersbach et al. 2020). This reanalysis operates using the ECMWF Integrated Forecast System (IFS) dynamical core and can provide meteorological information at relatively fine (0.25 degree hourly) resolution over the Earth. ERA5 provides both single-level and vertical profile information, allowing for comprehensive analyses of the atmospheric state. ERA5 data can be found at the Copernicus Climate Data Store (https://cds.climate.copernicus.eu/datasets).

While ERA5 can provide a comprehensive dataset of atmospheric conditions, particular focus was given to eight parameters: convective available potential energy (CAPE), total column water vapor (TCWV), column average temperature (Tavg), lifting condensation level height (zLCL), midlevel (850-500 hPa) lapse rate (mlLR), low-level (surface-850 hPa) lapse rate (llLR), low-level relative humidity (llRH) and deep-layer (surface-500 hPa) wind shear (dlWS). The first three parameters were identified in Chapter 3 and shown to have reasonable explanatory power regarding the ice characteristics of clouds and their effect on GPROF errors. The remaining five variables were identified by Schulte et al. (2024), which showed that these parameters can delineate the morphology of precipitating systems in the Tropics. While many other parameters can provide additional information, keeping focus on these eight allows for a more manageable description of the environment while also incorporating many important atmospheric processes. CAPE and TCWV are native variables in ERA5, while the remaining six are derived from other available ERA5 parameters. Column average temperature is calculated as the mean temperature in the atmospheric column, in this case from 1000 to 100 hPa (L=27 levels), as shown in Eq. 4.1. The lapse rates are calculated per Eq. 4.2 as the change in temperature over a given depth of the atmosphere. For llLR, T_1 and z_1 are for 850hPa while T_0

and z_0 are for the surface. Wind shear is calculated per Eq. 4.3 as the difference in wind speed between 500hPa and the surface. The LCL height and relative humidity were calculated using functions intrinsic to the MetPy Python module. These parameters were taken three hours prior to the associated GPROF precipitation to avoid the effects of airmass modification associated with precipitating systems.

$$Tavg = \frac{1}{L}\sum_{l=1}^{L} T_l \tag{4.1}$$

$$LR = \frac{(T_1 - T_0)}{(z_1 - z_0)} \tag{4.2}$$

$$WS = W_{500} - W_{sfc} \tag{4.3}$$

4.2.4 Data Processing

The data utilized in this study was taken during Water Year 2019 (October 2018-September 2019) for four regions of interest (ROIs): the Amazon (AMZN), Congo (CNGO), Southeast Asia (SEAS) and Southeast United States (SECONUS), as shown in Figure 4.1. AMZN and CNGO are well-known for exhibiting opposite error characteristics of each other in GPROF despite their relatively similar climatological precipitation characteristics (Petkovic and Kummerow 2017), while SEAS and SECONUS provide additional regions by which to assess GPROF errors. Additionally, the use of tropical and midlatitude ROIs provides an opportunity to assess the generalizability of the study. The radar and ERA5 data were matched to the GPROF resolution. For the radar products, the data were averaged into the footprint resolution of GPROF, while the ERA5 parameters were assigned to a given GPROF footprint using nearest neighbors. Additionally, the footprints utilized in this study were only considered if they were located over land. This was done by filtering the data based on the GPROF surface classes. For AMZN, CNGO and SEAS, footprints associated with surface classes 3 (max vegetation) and 17 (mountain rain) were retained. For SECONUS, surface classes 3-7 (max to min vegetation) and 17 were retained.

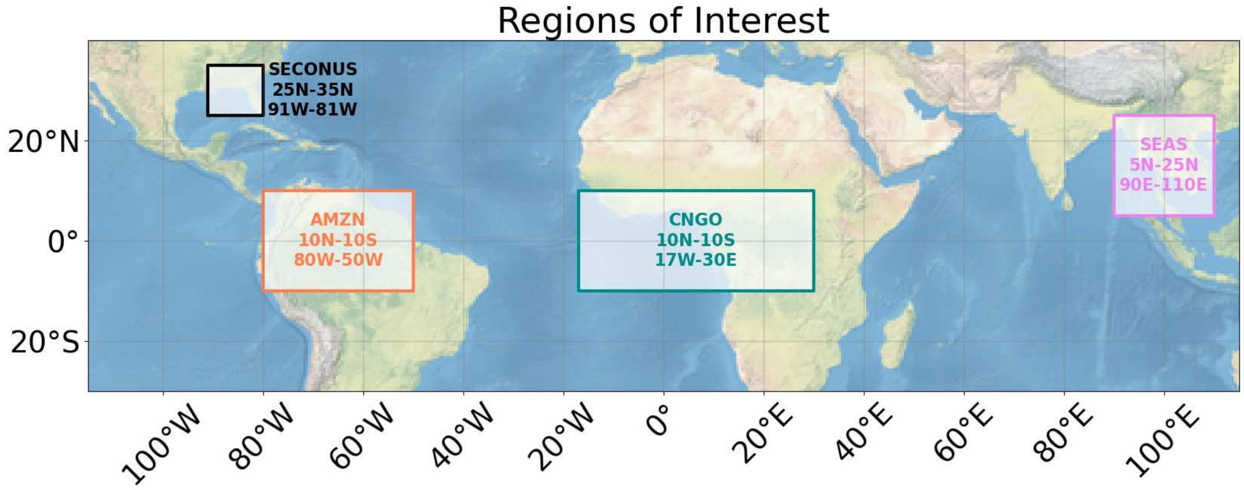

Fig 4.1: The regions of interest (ROIs) used in this study. In these ROIs, only those observations over land were utilized.

The error statistic which will be evaluated in this study is bias ratio. This statistic, as shown in Equation 4.4 is the ratio between the accumulated GPROF precipitation and an accumulated reference precipitation. For the Amazon, Congo and Southeast Asia, the reference precipitation comes from the GPM Combined algorithm, while for the Southeast United States the reference comes from MRMS. This representation of error has some advantages over other descriptions. First, its use of accumulated precipitation means that the calculation can be scaled to any spatiotemporal resolution without changing the calculation, making it applicable to errors at any resolution. Also, this error statistic can be inverted and used as a correction factor for the precipitation product. This provides a straightforward method by which to quantify the effect of accounting for errors attributable to different phenomena.

$$bias\ ratio = \frac{\sum RR_{GPROF}}{\sum RR_{REF}} \tag{4.4}$$

4.3 Satellite PRecipitation Errors from Ancillary Data (SPREAD) Model

4.3.1 Model Overview

To investigate the use of ERA5 information to estimate GPROF bias ratios, the Satellite Precipitation Errors from Ancillary Data (SPREAD) model was developed. SPREAD utilizes support vector regression (SVR) to best fit the ERA5 data to the bias ratios associated with each GPROF footprint. SVR, first introduced by Drucker et al. (1996), is a supervised learning technique which fits a nonlinear function to a high-dimensional feature dataset to predict a given response variable. Such a technique allows the features to be mapped to the response variable along a hyperplane, whereupon linear regression is used to locate individual samples and estimate the response (Smola and Scholkopf 2004; Zhang and O'Donnell 2020). An additional benefit of this technique is that it does not assume a pre-existing relationship between the feature set and the response variable. In this way, the exact relationship between the features and the response need not be known beforehand, which is of particular benefit to this problem as those relationships are still being understood.

Support vector regression utilizes kernel functions to determine the optimal fit for the feature data. For SPREAD, the radial basis function (Broomhead and Lowe 1988) was chosen. This kernel, which evaluates the distance a given vector set is from a reference point, is the most flexible of the functions typically used in support vector. It is particularly useful in cases where the exact relationships between the features and response variable are not known, as this kernel type makes no assumptions on the prior functional fit of the data. Additionally, support vector regression carries two free parameters: the regularization criteria (C) and the acceptable distance from the hyperplane (epsilon). These parameters control the hyperplane fitting, maximizing the number of samples which fall along the hyperplane while minimizing misclassifications.

SPREAD was trained using retrieval-scale information from the Amazon, Congo and Southeast Asia. This dataset consisted of the eight ERA5 parameters previously described as well as the GPPROF precipitation rates themselves. Including the GPROF precipitation rates was decided due to the well-known average state issue inherent to all retrievals, in which a considerable amount of error can be attributed to the tendency of satellite precipitation products to push its estimates toward the mean precipitation rate. Before use, this dataset was restricted to GPROF precipitation rates between 0.125 and 32 mm/hr and bias ratios of 0.1 to 10 to preserve the mean behaviors within the dataset and prevent contamination by extreme outliers. To ensure an insulated testing dataset, data from July 2019 were first set aside, then the remaining data were divided into training and validation sets with a randomized 80/20 split. This resulted in 41,690 samples for training, 10,423 samples for validation and 4,788 for testing datasets. The features were also standardized before ingestion into SPREAD to eliminate scale mismatches. Sample weights were also developed to improve the model's representation of the full bias range. These weights were developed using the absolute value of the standardized log-scaled bias ratios, as shown in Equation 4.5. These weights were applied with the intention of increasing the importance of samples with strong bias ratios (i.e. 0.1 or 10) as opposed to those which are effectively unbiased (i.e. near 1). Additional hyperparameter tuning through multiple 5-fold k-cross validation configurations was also undertaken to optimize the two free parameters, yielding a C value of 31.623 and an epsilon value of 0.5.

$$weights = 1 + \left| \frac{\log(BR) - \overline{\log(BR)}}{\sigma_{\log(BR)}} \right| \tag{4.5}$$

4.3.2 Model Performance Evaluation

Following the training and tuning steps, SPREAD's performance was evaluated over the training and validation datasets. The statistical evaluation utilized four parameters, shown in Equations 4.6 - 4.9: Pearson correlation (CORR), coefficient of determination (R2), mean absolute error (MAE) and root mean squared error (RMSE). In these equations, $BR_{i,true}$ is the true bias ratio for a GPROF footprint, $BR_{i,pred}$ is the predicted bias ratio for a GPROF footprint, n is the number of samples, $\overline{BR_{true}}$ is the mean of the true bias ratio and $\overline{BR_{pred}}$ is the mean of the predicted bias ratio. Table 4.1 provides these statistics for the tropical ROI datasets. Over the training and validation datasets, the correlation values are around 0.5, which shows that SPREAD is reasonably capable of predicting GPROF biases. The R2 values corroborate this, as the model captures around 17-25% of the variance in the bias ratio between the datasets. Since the bias ratio datasets have a mean value of around 0.97, MAE values of around 0.7 and RMSE values around 1 show that the error range of the model encompasses a substantial range of biases. Though this does raise questions as to the applicability of SPREAD, the model is able to reasonably capture the overall behaviors of the bias ratio correctly.

$$CORR = \frac{\sum\left(BR_{i,true} - \overline{BR_{true}}\right)\left(BR_{i,pred} - \overline{BR_{pred}}\right)}{\sqrt{\sum\left(BR_{i,true} - \overline{BR_{true}}\right)^2 \sum\left(BR_{i,pred} - \overline{BR_{pred}}\right)^2}} \tag{4.6}$$

$$R2 = 1 - \frac{\sum(BR_{i,true} - BR_{i,pred})^2}{\sum(BR_{i,true} - \overline{BR_{true}})^2} \tag{4.7}$$

$$MAE = \frac{1}{n}\sum\left(BR_{pred} - BR_{true}\right) \tag{4.8}$$

$$RMSE = \sqrt{\frac{1}{n}\sum\left(BR_{pred} - BR_{true}\right)^2} \tag{4.9}$$

Table 4.1: SPREAD performance statistics over the training, validation and testing data from the tropical ROIs and the testing data from the Southeast United States.

	CORR	R2	MAE	RMSE
Training Data	0.521	0.252	0.684	1.005
Validation Data	0.505	0.224	0.687	1.003
Tropics Test Data	0.503	0.174	0.737	1.081
CONUS Test Data	0.433	-1.791	0.938	1.304

These performance statistics can also be visualized to provide additional context to SPREAD's capability to predict GPROF biases. Figure 4.2 does this through a two-dimensional histogram of the truth and predicted biases for both the training and validation datasets. First and foremost, the moderately positive relationship between the true and predicted biases is evident in both datasets, indicating that SPREAD does produce bias predictions which are reasonably in line with expectations. Within the main mode of the data, as indicated by the highest densities, it appears that SPREAD provides bias predictions with reasonable accuracy, though a slight overestimation tendency is observed. Looking at the samples outside this main signal, SPREAD tends to overestimate biases less than 1 and underestimate biases greater than 1. SPREAD rarely predicts biases below 0.5 or above 2, which is likely a result of the considerably higher point densities within this range, while the true biases occupy a much larger range. Because of this tendency, SPREAD struggles to predict the more extreme biases in the dataset. Still, this visualization does show SPREAD performs reasonably well over the bulk of the dataset.

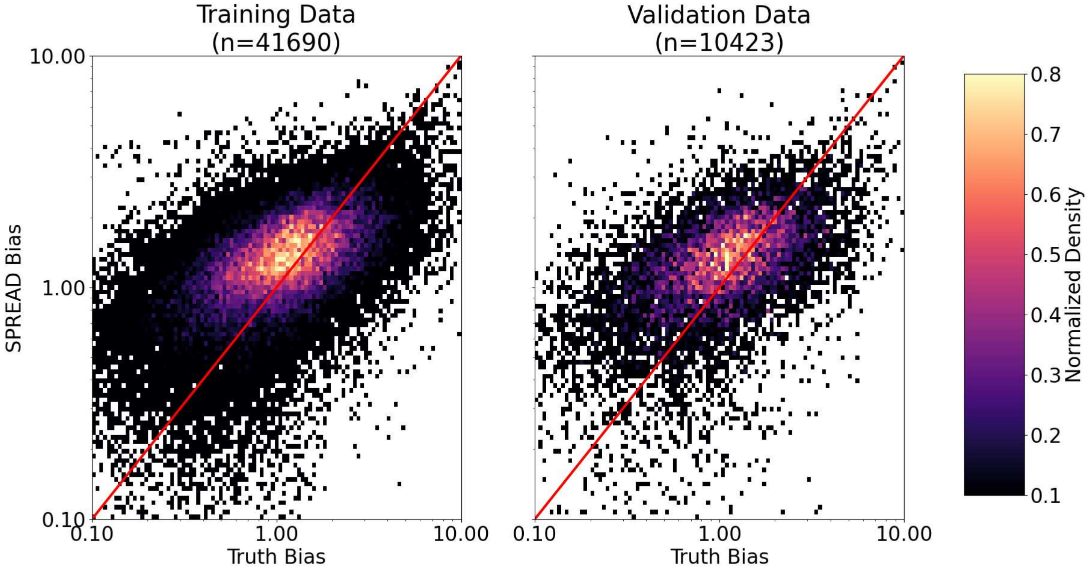

Fig 4.2: Two-dimensional histograms of the true vs SPREAD-predicted bias for the (left) training and (right) validation datasets. The red diagonal line represents a perfect predictor.

To investigate which ERA5 parameters were most useful to SPREAD, permutation feature importance analysis was performed and shown in Fig. 4.3. This analysis assesses the impact a given predictor has on SPREAD's performance if that variable was randomized. From the figure, it is apparent that all the input parameters were important to the model's performance, with the weakest contributor still achieving a change in the training accuracy above 0.2. Despite this, there appear to be well-defined groups of parameters which show varying amounts of importance. The first of these groups includes zLCL, TCWV and Tavg, all of which provide information on the low-level thermodynamic structure of the atmosphere. Though TCWV and Tavg are vertically integrated parameters, the bulk of their signal is attributable to the lower atmosphere and thus they can be considered as predominantly a lower atmospheric signal. The next group includes llLR and llRH, which again describe low level thermodynamics. Also, these two parameters appear to occupy a very similar range of effects on the model accuracy, which may suggest that one of these parameters could be removed to reduce the redundant information in the model. The following group includes GPROF, mlLR and CAPE, which mostly describe mid-atmospheric conditions. Like with the previous group, there is considerable overlap between these features, which may suggest some redundancy in the information provided by these variables. Finally, dlWS comprises the final group and is the only kinematic parameter in the dataset. This result seems to indicate that such information is not as important as that from the thermodynamics of the system.

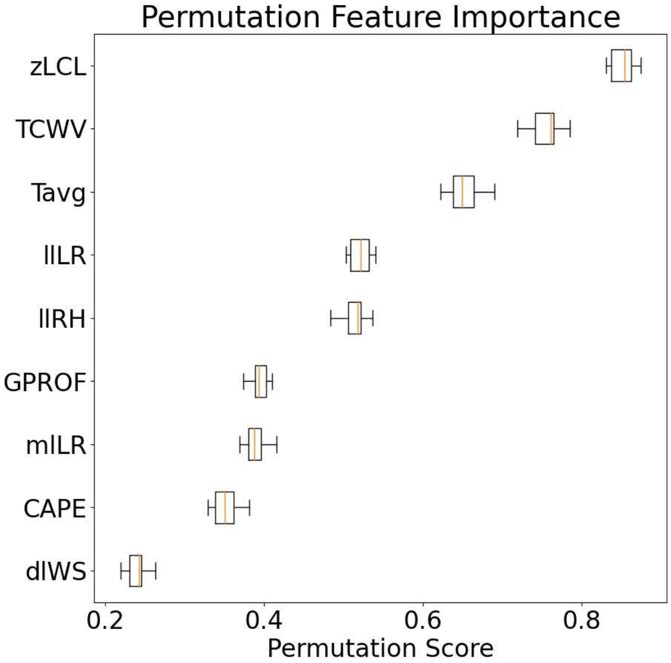

Fig 4.3: Permutation feature importances for the input parameters in SPREAD. Larger values indicate greater importance to model accuracy.

4.4 Results

4.4.1 Application to Tropical Precipitation

Following the evaluation of the SPREAD model over the training and validation datasets, its performance in the July 2019 testing data was investigated. Statistically, the model shows only negligible differences from the training and validation datasets, with a CORR of 0.503, an

R2 of 0.174, an MAE of 0.737 and an RMSE of 1.081. This indicates that within the Tropics, SPREAD generalizes quite well. This agreement is also reflected in Figure 4.4, which displays very similar characteristics as those shown in Figure 4.2. One notable departure from the training and validation datasets is the increased amount of scatter. While this may be related to the low sample size of this dataset, it is also possible that isolating a specific month from the time series may introduce some time-dependent variability in these data that is not fully captured in the model.

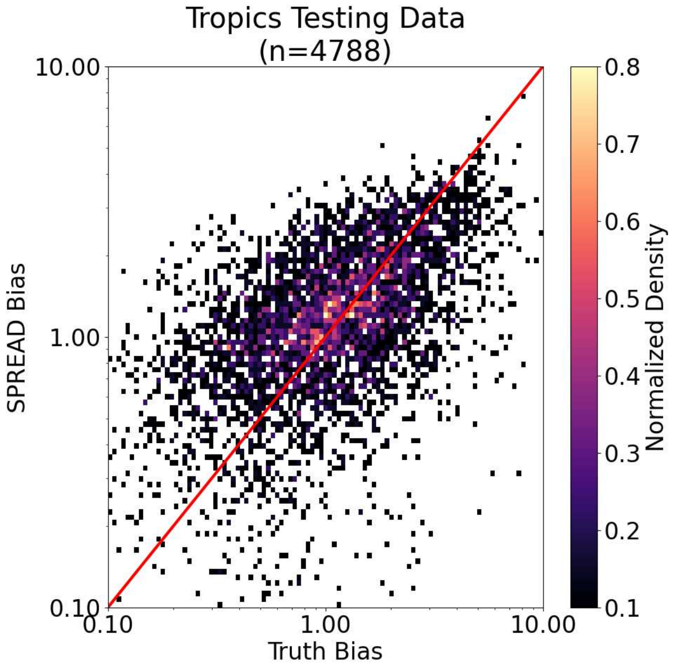

Fig 4.4: The same as Figure 4.2, but for the testing dataset from the July 2019 tropical ROI data.

While evaluating SPREAD's statistical performance is useful, evaluating the model over individual scenes can provide more context. Figures 4.5 and 4.6 provide some examples from this analysis. Using these examples, it is apparent that SPREAD's performance can vary considerably by orbit but overall captures the expected behaviors. Looking first at Figure 4.5, it appears that SPEAD does well at predicting the bias ratio. The large area of underestimation near the center of the scene is recreated well, though the magnitudes of the biases in SPREAD are smaller than in the truth data. The stronger overestimation tendency in the northern portion of the scene is also reasonably recreated and even appears to assess the magnitude of the bias correctly. Elsewhere, SPREAD does seem to have trouble establishing the severity of the biases, as many of the footprints here have values close to 1 in the SPREAD predictions while the truth shows greater heterogeneity. This behavior appears to be a systematic issue as evidenced by the tendency of SPREAD to constrain its predictions to a much narrower range of biases than the truth and is an area of improvement for this model. These behaviors are also quite similar to those in most of the orbits analyzed, indicating that overall SPREAD is reliable at capturing the type of bias expected.

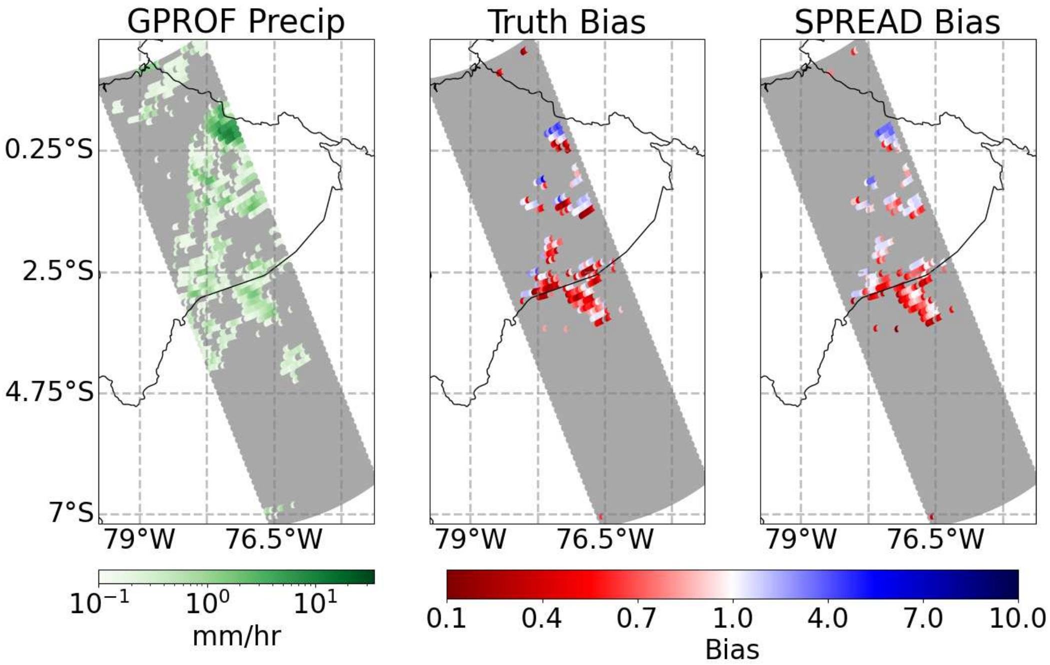

Fig 4.5: An example orbit from the July 2019 tropical testing dataset. Areas in gray indicate missing information. The leftmost panel shows the GPROF precipitation rate, the center panel shows the expected bias and the rightmost panel shows the SPREAD-predicted bias.

Moving to Figure 4.6, SPREAD appears to be less adept at predicting biases here. Of particular interest is the precipitation feature centered at roughly 1 South, where SPREAD predicts overestimation in an area mostly characterized by underestimation. This discrepancy is strongly associated with heavy precipitation, which may indicate a potential issue in using this model during these events. Since heavy precipitation is a rare occurrence, it is possible that during the model fitting process, SPREAD did not encounter a large enough number of these events to fully capture their bias characteristics. Also, SPREAD does generally show a systematic overestimation bias in its predictions, which may be compounding the difficulties in this scene, elucidating areas where the model could be improved.

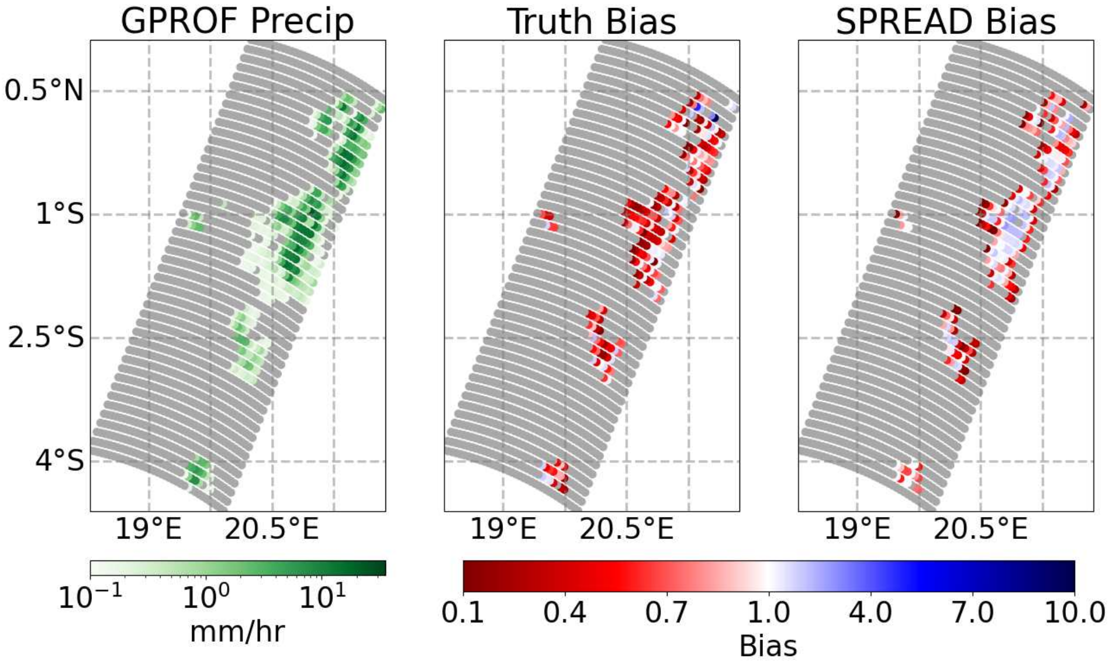

Fig 4.6: The same as Figure 4.5, but for a different orbit segment in the dataset.

4.4.2 Application to Midlatitude Precipitation

While SPREAD was trained purely on information from the Tropics, additional testing was performed in the Southeast United States to assess the model's applicability to midlatitude precipitation. This region was chosen because of its extensive ground truth in the MRMS data as well as the potential to experience weather patterns like those found in the Tropics. To ensure only the highest quality information from the MRMS data was utilized in this portion of the study, only those footprints with a radar quality index (RQI) of 1 and hail and snow fractions less than 0.5 were considered. This leaves only 6,131 samples from SECONUS for examination, presenting a potential data volume issue. This investigation takes the same approach as Section 4.4.1, looking at SPREAD's performance in this region. In the statistical evaluation, SPREAD performs noticeably worse with these data, yielding a CORR of 0.433, an R2 of -1.791, an MAE of 0.938 and an RMSE of 1.304. The negative R2 value is particularly concerning, as this would indicate that SPREAD performs worse than a persistence model at predicting bias. Since a persistence model would predict the mean value of the dataset, this result indicates that SPREAD is experiencing considerable systematic errors which result in an inability to recreate the mean bias of the data. The remaining statistics, however, seem to indicate that SPREAD is not entirely incapable of predicting biases in SECONUS, with a weak but positive correlation of 0.43 indicating some ability. As such, the use of this model outside of the Tropics shows potential but requires further work to improve its performance.

Figure 4.7 shows the performance as a two-dimensional histogram. From this figure, it is apparent that SPREAD consistently overestimates the bias in this region, which likely explains the negative R2 value. The highest densities in this figure indicate this quite well, with SPREAD tending to predict a bias ratio a little greater than 1 where the truth data indicates bias ratios of around 0.7, which amounts to a roughly 40% error in the prediction. Like with the Tropics data, SPREAD favors a much narrower range of biases (0.6-2) than is present in the truth data, again highlighting the model's struggle to represent the full range of errors. This figure also shows a much larger amount of scatter than with the tropical regions, further highlighting SPREAD's struggles with this dataset. Despite these issues, the figure does show a semblance of a positive relationship between the true and predicted biases, reaffirming the model's potential here.

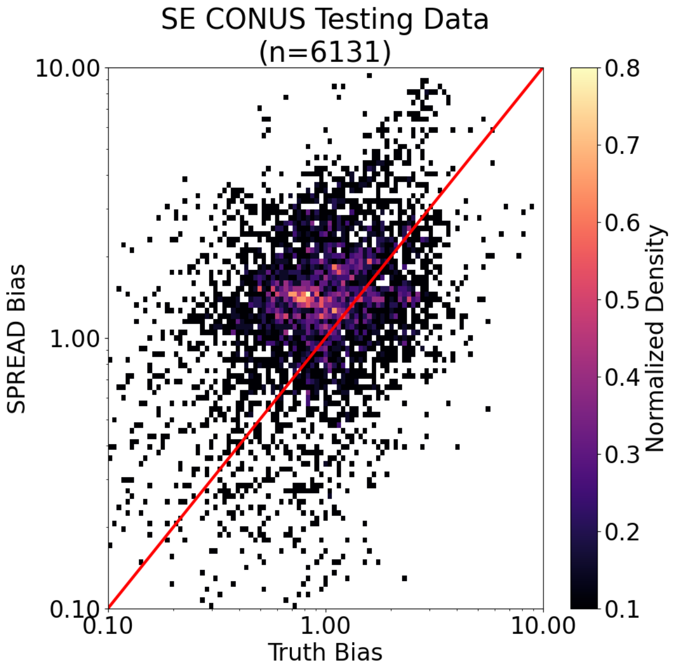

Fig 4.7: The same as Fig 4.2, but for the Southeast United States testing dataset.

Additionally, SPREAD's performance on individual scenes over the Southeast United States was investigated. Figures 4.8 and 4.9 provide examples of this analysis. Looking first at Figure 4.8, many of the previously identified issues can be identified. Much of the main precipitation structure exhibits the systematic overestimation error in the SPREAD predictions, with moderate overestimation predicted in areas which are relatively unbiased in the truth data such as that near 32 North. This systematic overestimation again appears to be associated with enhanced precipitation, corroborating SPREAD's difficulty with heavy precipitation events described previously. The opposite effect is also notable in the northernmost precipitation structure in the scene, where SPREAD predicts strong underestimation bias where the truth indicates a relatively unbiased solution. Figure 4.9, on the other hand, shows an instance of much better performance by SPREAD, though many of the previously outlined complications remain. The bias characteristics are captured well by the model, especially in the feature centered near 33 North, though it again shows a strong preference for predicting an underestimation bias over light precipitation and an overestimation bias for heavier precipitation. The systematic overestimation error in the model remains evident, as the predicted biases are consistently closer to overestimation than they are in the truth data. Based on these results, the SPREAD model does not generalize particularly well, though its encouraging performance statistics and potential to assess biases in individual scenes show it has promise.

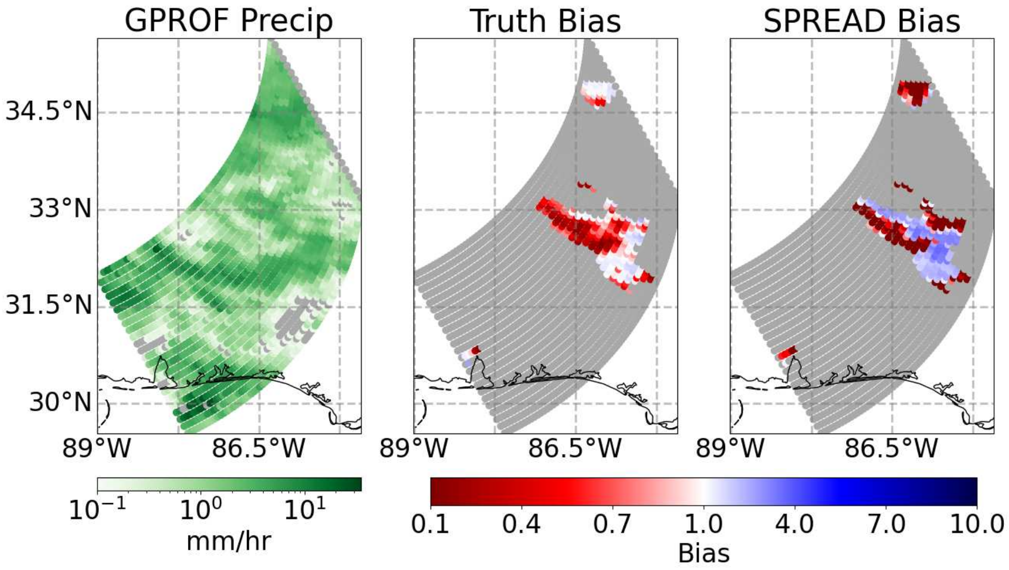

Fig 4.8: An example orbit segment from the Southeast United States testing dataset. The panel configuration is identical to that in Fig 4.5.

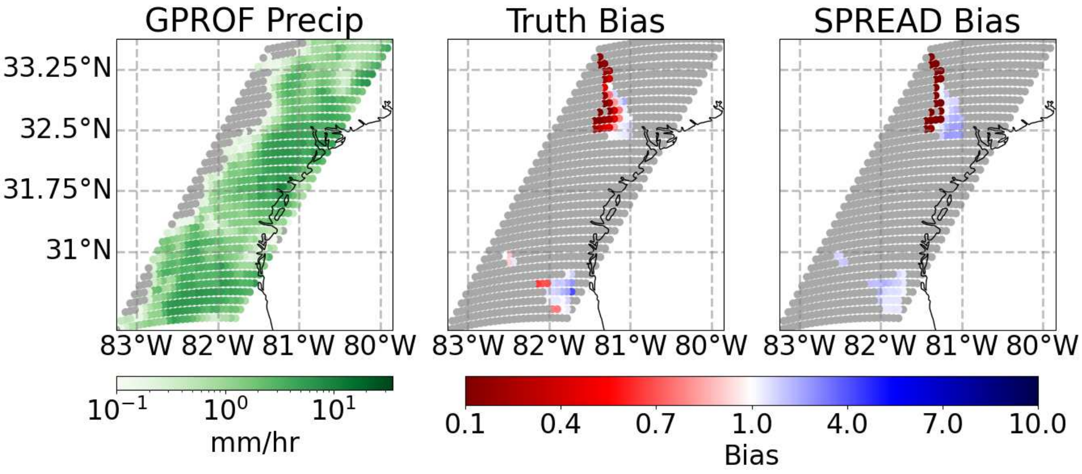

Fig 4.9: The same as Fig 4.8, but for a different orbit segment in the testing database.

4.4.3 Scale Sensitivity and Effective Resolution for Bias Constraint

While SPREAD shows promise in predicting retrieval-scale biases both in tropical and midlatitude regions, it remains to be seen at what spatiotemporal scale it is most effective. To that end, a scale sensitivity analysis was undertaken. Four total iterations of SPREAD were trained using data at multiple levels of aggregation, as detailed in Table 4.2. The EX_IF experiment is identical to the initial model configuration, while the remaining configurations ingest data at the various listed resolutions, which were developed by aggregating the GPROF footprint data. These data were each then separated and standardized using the process described previously to ensure consistency in comparison. Due to its already small sample size, this analysis does not include the Southeast United States data. To avoid a dependency on the hyperparameter tuning, these experiments were conducted using the default hyperparameters in the scikit-learn SVR function (C = 1; epsilon = 0.1).

Table 4.2: Descriptions for the model configurations to test SPREAD's resolution sensitivity.

	EX_IF	EX_MS	EX_LS	EX_SS
Description	Retrieval scale	Mesoscale	Synoptic scale	Sub-seasonal scale
Timescale	instantaneous	hourly	daily	monthly
Grid Resolution	11x18km irregular	0.25 degree regular	0.5 degree regular	1.0 degree regular

To test the effectiveness of SPREAD at each of these resolutions, the model was retrained for each experiment and their statistical performances were compared. Figure 4.10 shows this comparison using the four statistical parameters from the performance evaluation. The EX_IF configuration is the most accurate model configuration overall, with correlations near 0.5, R2 values of at least 0.2, MAE values near 0.6 and RMSE values near 1. This configuration, however, exhibits behaviors associated with underfitting, as the training dataset shows worse performance than the validation and testing data. Both EX_MS and EX_SS show unstable behaviors, with inconsistent performance metrics across the training, validation and testing datasets. This is especially apparent in R2, where EX_MS ranges between 0.05 and 0.15 and EX_SS between 0.1 and 0.2. EX_LS appears to be the most stable of the model configurations, with small differences between the datasets and a slight tendency towards overfitting. These results, alongside with its modestly degraded accuracy compared to EX_IF indicate that the SPREAD model is most effective at the 0.5-degree daily resolution. This is not entirely surprising, as the resolution of ERA5 allows it to best resolve phenomena at this scale. It is possible that training SPREAD with another model as input would affect these results based on that model's resolution. Nevertheless, the performance characteristics described show that it is possible to utilize SPREAD at multiple resolutions, but in its current configuration a 0.5-degree daily resolution provides an optimal balance between model stability and accuracy.

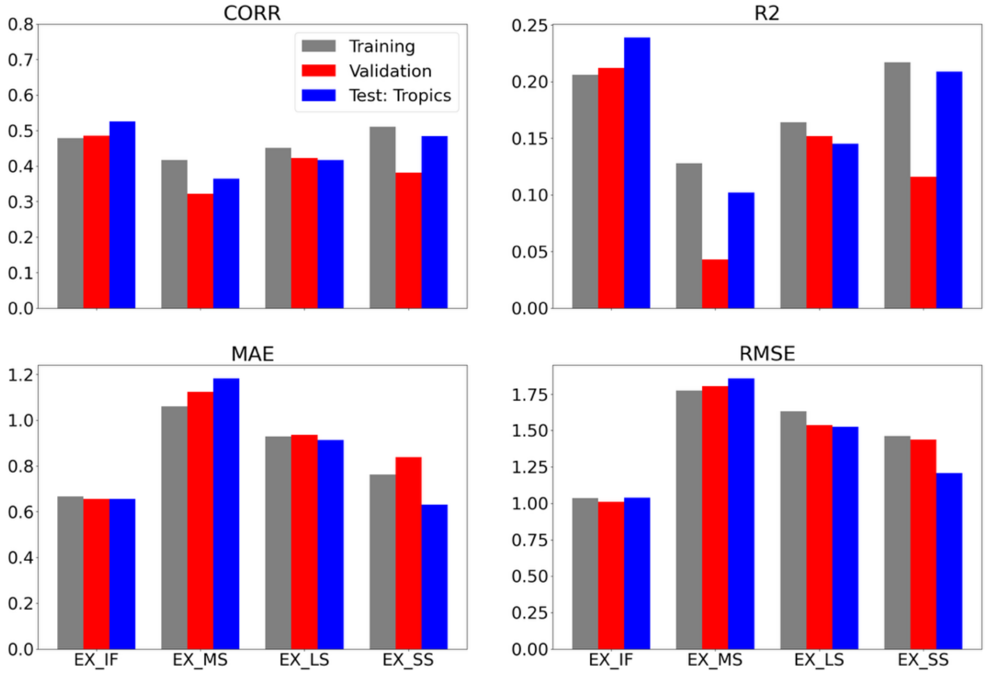

Fig 4.10: The performance statistics for each experimental resolution configuration for SPREAD. Each panel is an individual statistic and the three-bar groups in each panel represent a different configuration.

4.5 Discussion and Conclusions

Satellite precipitation products can provide global-scale information on rainfall but lack quantifiable global errors due to the sparsity of high-quality reference data. Since precipitating systems are a product of their environment, this information provides an area of opportunity to fill the gaps in these traditional analyses. To this end, the SPREAD model was developed, taking information on the large-scale environment from ERA5 to predict satellite precipitation biases over the Amazon, Congo, Southeast Asia and Southeast United States.

In the tropical regions where SPREAD was trained, the model performs reasonably well, with correlations of around 0.5 and R2 values between 0.17-0.25 showing that the model has some skill in predicting bias. Individual orbit analyses corroborate this, with the cases of overestimation and underestimation located mostly correctly, though SPREAD's inability to fully capture the bias range results in consistently low bias magnitudes. Over the Southeast United States, however, SPREAD struggles to predict bias. A correlation of 0.43 indicates some degradation in SPREAD's performance compared to the Tropics but does still signal some capability. A negative R2 value, however, indicates that the model is not reliable in this region and thus should be treated with caution. This is reflected in the individual orbits as well, with frequent misrepresentations of the biases contained within them. Nevertheless, SPREAD does show potential in predicting biases in SECONUS, indicating that with improvement the model may generalize to other regions.

Additional analysis of SPREAD was undertaken to determine which environmental characteristics most strongly impact its performance as well as the optimal resolution at which to use the model. Investigations of the feature importances indicate that SPREAD is most strongly affected by lower atmosphere thermodynamics. The LCL height, TCWV and Tavg dominate the feature importances in SPREAD, while the GPROF precipitation, CAPE and wind shear occupy a less prominent role. The sensitivity of SPREAD to the resolution of its input data was also investigated by training multiple model configurations for different baseline spatiotemporal resolutions. From these tests, SPREAD's performance optimized at 0.5-degree daily scale, as determined from the relatively good statistical performance as well as the consistency in these metrics across the various datasets involved. This scale is an ideal resolution for synoptic-scale features, which is consistent with the resolution capabilities of ERA5. Since these results are largely related to the resolution and constraints associated with the feature dataset, the use of a different reanalysis may alter these results.

While this model does show promise in providing error information for satellite precipitation, considerable work must still be undertaken before it can be used in the broader research and operations spheres. First and foremost, the degradation in model performance noted in the transition from tropical to midlatitude precipitation must be addressed. The easiest method of addressing this limitation would entail training SPREAD on data from both the tropics and midlatitude as opposed to only one of these areas. This task would have to be performed with the GPM Combined information as the truth dataset, however, which is less than ideal compared to a high-quality ground-based dataset like that for MRMS. Conversely, it may be beneficial to develop separate configurations of SPREAD for tropical and midlatitude precipitation, allowing the model to specialize in those systems and thus perform better in the respective regions.

Another limitation is the feature dataset, which while inclusive of several atmospheric processes, would likely benefit from additional information. In its current iteration, the feature database leans heavily on the thermodynamic characteristics of the environment, though kinematic processes are also important for developing weather systems. This abstention may be reasonable for the Tropics, which tend to have weaker dynamical forcings, but this is not true for the midlatitudes. As such, the inclusion of additional kinematic parameters like vertical velocity and mass divergence may provide beneficial information to the model. Aside from including additional parameters, feature engineering, through anomalies and/or feature combinations may also provide additional information for SPREAD and are another area of improvement.

Despite these limitations, the development of SPREAD and its performance across tropical and midlatitude precipitation regimes indicates that it is possible to identify the errors in satellite precipitation products using information on the large-scale environment. Since such information can be gathered globally, it is thus possible to develop estimates of bias in the absence of a reliable reference data. This can complement traditional ground validation, providing information to the data sparse regions of the world which need them the most.

CHAPTER 5: CONCLUSIONS

Errors in satellite precipitation products, though highly variable in space and time, can be attributed to the shortcomings of the assumptions made regarding the geophysical characteristics of the precipitating systems. While there has been much work on identifying the meteorological conditions which support or suppress precipitation as well as identifying satellite precipitation product errors under specific circumstances, none have worked to leverage our knowledge of how the atmosphere produces precipitation to understand these errors in a broader sense. This dissertation provides one perspective by which to bridge this gap, presenting novel investigations of the relationship between satellite precipitation errors and the underlying meteorology in which they occur. This has been done by (i) identifying the radar-derived information which describes the radiative characteristics used by satellite precipitation products and how these characteristics contribute to errors, (ii) developing a proxy for the ice characteristics observed by radars which solely utilized information on the large-scale environment, and (iii) providing a potential method to predict satellite precipitation errors using interpretable meteorological information.

The first part of this dissertation investigated the individual assumptions within the GPROF algorithm as potential sources of bias. Using information gathered from three tropical regions, the biases in GPROF were first identified and then related to hydrometeor characteristics as determined by the GPM Combined algorithm. From this investigation, three main error sources were identified. The first was the average state assumption, in which the retrieval algorithm tends to drive its estimates towards the mean of the dataset and causes overestimation at low precipitation rates and underestimation at high precipitation rates. The second was the ice scattering assumption, which states that as the amount of ice increases, the algorithm tends to inflate the precipitation intensity, leading to overestimates of precipitation in heavily ice-laden systems and underestimates in cases with little to no ice. The third was a collection of second-order effects which largely describe the inability of the satellite information to interrogate the lower levels of the atmosphere. These error sources were found to be observable in the CMB data, specifically the precipitation intensity and ice-rain ratio, as well as radiometer information in the polarization correct 37GHz brightness temperatures. By using these three parameters to identify and account for the bias under certain conditions, a roughly 70% improvement in bias consistency was achieved, showing that a large amount of these biases is controlled by a few major sources which can be identified by physical parameters.

The second part of this dissertation developed the connection between the ice properties of precipitating systems and the environments in which they occur. The ice properties became the focus of this analysis due to their known and inherent dependence on the incident environment, as opposed to the other error sources which were either mathematical artifacts or too obscure to definitively attribute. Using a seven-year time series of tropical precipitation and ice hydrometeor characteristics, five ice scattering regimes were developed via K-Means clustering. These regimes were developed at very large scales and were found to describe different system morphologies, ranging from shallow stratiform systems to monsoonal flows to deep organized convection. Comparisons with matched data from ERA5 showed that CAPE, TCWV and Tavg could be used to identify which ice regime was likely present. Efforts to reconstruct the ice regimes from these variables showed promise, with the full combination of parameters showing promise in identifying which regime a given observation belongs to. These regimes, both with the ice data and as developed from ERA5, also proved to be capable of constraining GPROF biases in a similar manner as with the actual ice hydrometeor information, again showing a 50-70% improvement in the regional constraint.

The third part of this dissertation endeavored to develop a direct quantification method for bias solely utilizing geophysical information. To do this, the SPREAD model was developed, which utilized support vector regression to translate a set of ERA5 parameters and GPROF precipitation rates into bias. This model, trained and tuned with information from the Tropics, was found to perform reasonably well for predicting these biases, with moderately positive correlations and large but manageable errors. When moved to the midlatitudes, specifically the Southeast United States, SPREAD was much less adept at characterizing GPROF biases but was still found to exhibit the potential to do so both through its performance statistics and investigations into individual scenes. Feature importance analyses suggest that meteorological information pertaining to the lower atmosphere are most important for determining bias, though further work should investigate additional parameters to complete this picture. SPREAD was also found to stabilize at a 0.5-degree daily resolution, indicating that this model is best applied to large-scale bias assessments, though it is possible to utilize other spatiotemporal resolutions depending on the desired outcome.

For much of this dissertation, particular focus was given to large-scale atmospheric phenomena and therefore the analyses performed were tailored to coarse resolution information and predictions. It is worth emphasizing that while these scales are much larger than the precipitation features themselves, the correspondence of the results found in Chapters 2 and 3 to known difficulties in satellite precipitation products and distinguishable atmospheric states signifies that these results are robust. As such, it is believed that these results can confidently be applied at the large spatiotemporal scales studied. Such applications may include climatological analysis of satellite precipitation, which is becoming possible given the length of the satellite data record. The results of Chapter 4, however, show the potential to extend these conclusions into resolutions with greater utility in precipitation forecasting applications, though at a much lower confidence than for a coarser mode of analysis. While not an exact conversion, the performance characteristics of the SPREAD model show that it is a possibility which should be explored more intentionally in future studies. Nonetheless, the dependence of precipitation on forcings at multiple scales shows that not only does the body of research undertaken in this dissertation need to be continued, but the information gathered from these analyses can inform these additional levels of research.

The results of this dissertation indicate that it is possible to diagnose satellite precipitation product errors using information relevant to the environment in which the precipitation formed. Since this body of research represents an initial attempt to provide a physical basis for assessing these errors in the absence of a reference dataset, considerable refinement is necessary to produce an operationally viable methodology. This includes but is not limited to testing over more regions of the world and examination of additional atmospheric processes which were not considered during the development of this work. Nevertheless, the results presented in this dissertation represent a path forward in developing globally available satellite precipitation error statistics regardless of the presence of ground truth data. Should this method or a similar one be developed with sufficient skill, it would provide considerable benefit to forecasters, who can use this information to evaluate the fidelity of satellite precipitation products in their respective regions, and the research community by facilitating investigations of product performance under specific scenarios and stabilizing the satellite data record for use in climatological applications. In all, this body of work increases our knowledge of and confidence in satellite precipitation data and provides an additional tool which can be used to investigate this important component of the global hydrologic cycle.

REFERENCES

Adhikari A., C. Liu, and L. Hayden, “Uncertainties of GPM microwave imager precipitation estimates related to precipitation system size and intensity,” J. Hydrometeorol., vol. 20, no. 9, pp. 1907–1923, Sep. 2019, doi: 10.1175/jhm-d-19-0038.1.

Adler R.F., G. Gu, and G. J. Huffman, “Estimating climatological bias errors for the global precipitation climatology project (GPCP),” J. Appl. Meteorol. Climatol., vol. 51, no. 1, pp. 84–99, Jan. 2012, doi: 10.1175/jamc-d-11-052.1.

Alcântara, C.R., Maria A.F. Silva Dias, Enio P. Souza, Julia C.P. Cohen, Verification of the role of the low level jets in Amazon squall lines, Atmospheric Research, Volume 100, Issue 1, 2011, Pages 36-44, https://doi.org/10.1016/j.atmosres.2010.12.023.

Berg W., T. L’Ecuyer, and C. Kummerow, “Rainfall climate regimes: The relationship of regional TRMM rainfall biases to the environment,” J. Appl. Meteorol. Climatol., vol. 45, no. 3, pp. 434–454, Mar. 2006, doi: 10.1175/jam2331.1.

Biswas S.K. and V. Chandrasekar, “Cross-validation of observations between the GPM dual-frequency precipitation radar and ground based dual-polarization radars,” Remote Sens., vol. 10, no. 11, p. 1773, Nov. 2018, doi: 10.3390/rs10111773.

Bogerd, L., Leijnse, H., Overeem, A., and Uijlenhoet, R.: Assessing sampling and retrieval errors of GPROF precipitation estimates over the Netherlands, Atmos. Meas. Tech., 17, 247–259, https://doi.org/10.5194/amt-17-247-2024, 2024.

Braga R. C. and D. A. Vila, “Investigating the ice water path in convective cloud life cycles to improve passive microwave rainfall retrievals,” J. Hydrometeorol., vol. 15, no. 4, pp. 1486–1497, Aug. 2014, doi: 10.1175/jhm-d-13-0206.1.

Broomhead, D.S., & Lowe, D. (1988). Multivariable Functional Interpolation and Adaptive

Networks. Complex Syst., 2.

Cauteruccio, A., Colli, M., Stagnaro, M., Lanza, L.G., Vuerich, E. (2021). In-situ Precipitation Measurements. In: Foken, T. (eds) Springer Handbook of Atmospheric Measurements. Springer Handbooks. Springer, Cham. https://doi.org/10.1007/978-3-030-52171-4_12

Cecil D. J. and T. Chronis, "Polarization-corrected temperatures for 10−, 19−, 37−, and 89-GHz passive microwave frequencies," J. Appl. Meteorol. Climatol., vol. 57, no. 10, pp. 2249–2265, Oct. 2018, doi: 10.1175/JAMC-D-18-0022.1.

Chen, T., W. Huang, and E. S. Takle, 2004: Annual Variation of Midlatitude Precipitation. J. Climate, 17, 4291–4298, https://doi.org/10.1175/JCLI3201.1.

Cohen J. C. P, M. A. F. S. Dias, and C. A. Nobre, "Environmental conditions associated with Amazonian squall lines: A case study," Monthly Weather Rev., vol. 123, pp. 3163–3174, Jan. 1995, doi: 10.1175/1520-0493(1995)123<3163:ECAWAS>2.0.CO;2.

Davis, J., Knippertz, P. and Fink, A.H. (2013), The predictability of precipitation episodes during the West African dry season. Q.J.R. Meteorol. Soc., 139: 1047-1058. https://doi.org/10.1002/qj.2014

Del Genio, A. D., and W. Kovari, 2002: Climatic Properties of Tropical Precipitating Convection under Varying Environmental Conditions. J. Climate, 15, 2597–2615, https://doi.org/10.1175/1520-0442(2002)015<2597:CPOTPC>2.0.CO;2.

Derin Y. and P. E. Kirstetter, "Evaluation of IMERG over CONUS complex terrain using environmental variables," Geophys. Res. Lett., vol. 49, no. 19, Oct. 2022, doi: 10.1029/2022gl100186.

Dezfuli A.K. et al., "Validation of IMERG precipitation in Africa," J. Hydrometeorol., vol. 18, no. 10, pp. 2817–2825, Oct. 2017, doi: 10.1175/jhm-d-17-0139.1.

Drucker, H., Burges, C. J., Kaufman, L., Smola, A., & Vapnik, V. (1996). Support vector regression machines. Advances in neural information processing systems, 9.

Dyer E. L. E. et al., “Congo basin precipitation: Assessing seasonality, regional interactions, and sources of moisture,” J. Geophys. Res., Atmos., vol. 122, no. 13, pp. 6882–6898, Jul. 2017, doi: 10.1002/2016jd026240.

Ebert, E.E. (2007). Methods for Verifying Satellite Precipitation Estimates. In: Levizzani, V., Bauer, P., Turk, F.J. (eds) Measuring Precipitation From Space. Advances In Global Change Research, vol 28. Springer, Dordrecht. https://doi.org/10.1007/978-1-4020-5835-6_27

Fattorelli, S., Fontana, G.D., Da Ros, D. (1999). Flood Hazard Assessment and Mitigation. In: Casale, R., Margottini, C. (eds) Floods and Landslides: Integrated Risk Assessment. Environmental Science. Springer, Berlin, Heidelberg. https://doi.org/10.1007/978-3-642-58609-5_2

Gebregiorgis A. and F. Hossain, "Making Satellite Precipitation Data Work for the Developing World," in IEEE Geoscience and Remote Sensing Magazine, vol. 2, no. 2, pp. 24-36, June 2014, doi: 10.1109/MGRS.2014.2317561.

Gimeno, L., A. Stohl, R. M. Trigo, F. Dominguez, K. Yoshimura, L. Yu, A. Drumond, A. M. Durán-Quesada, and R. Nieto (2012), Oceanic and terrestrial sources of continental precipitation, Rev. Geophys., 50, RG4003, doi:10.1029/2012RG000389.

Goldenstern E. and C. Kummerow, “Predicting region-dependent biases in a GOES-16 machine learning precipitation retrieval,” J. Appl. Meteorol. Climatol., vol. 62, no. 7, pp. 873–885, Jul. 2023, doi: 10.1175/jamc-d-22-0089.1.

Goldenstern, E.M., and C. D. Kummerow, "Understanding Regional Passive Microwave

Precipitation Bias Using Radar-Derived Information," in IEEE Transactions on Geoscience and Remote Sensing, vol. 62, pp. 1-9, 2024, Art no. 4110509, doi: 10.1109/TGRS.2024.3470552.

Grecu M. et al., “The GPM combined algorithm,” J. Atmos. Ocean. Technol., vol. 33, no. 10, pp. 2225–2245, Oct. 2016, doi: 10.1175/JTECHD-16-0019.1.

Gu, G., and R. F. Adler, 2004: Seasonal Evolution and Variability Associated with the West African Monsoon System. J. Climate, 17, 3364–3377, https://doi.org/10.1175/1520-0442(2004)017<3364:SEAVAW>2.0.CO;2.

Hersbach H, Bell B, Berrisford P, et al. The ERA5 global reanalysis. Q J R Meteorol Soc. 2020;146: 1999–2049. https://doi.org/10.1002/qj.3803

Hossain F. and E. N. Anagnostou, "A two-dimensional satellite rainfall error model," in IEEE Transactions on Geoscience and Remote Sensing, vol. 44, no. 6, pp. 1511-1522, June 2006, doi: 10.1109/TGRS.2005.863866.

Hou, A. Y., and Coauthors, 2014: The Global Precipitation Measurement Mission. Bull. Amer. Meteor. Soc., 95, 701–722, https://doi.org/10.1175/BAMS-D-13-00164.1.

Hsiao, W., E. D. Maloney, N. M. Leitmann-Niimi, and C. D. Kummerow, 2024: Observed Relationships between Sea Surface Temperature, Vertical Wind Shear, Tropical Organized Deep Convection, and Radiative Effects. J. Climate, 37, 1277–1293, https://doi.org/10.1175/JCLI-D-23-0262.1.

IPCC, 2023: Sections. In: Climate Change 2023: Synthesis Report. Contribution of Working Groups I, II and III to the Sixth Assessment Report of the Intergovernmental Panel on Climate Change [Core Writing Team, H. Lee and J. Romero (eds.)]. IPCC, Geneva, Switzerland, pp. 35-115, doi: 10.59327/IPCC/AR6-9789291691647

Jollyta, D., S. Efendi, M. Zarlis, H. Mawengkang (2023) Analysis of an optimal cluster approach: a review paper. J. Phys.: Conf. Ser. 2421 012015, doi: 10.1088/1742-6596/2421/1/012015.

Kochendorfer, J., Rasmussen, R., Wolff, M., Baker, B., Hall, M. E., Meyers, T., Landolt, S., Jachcik, A., Isaksen, K., Brækkan, R., and Leeper, R.: The quantification and correction of wind-induced precipitation measurement errors, Hydrol. Earth Syst. Sci., 21, 1973–1989, https://doi.org/10.5194/hess-21-1973-2017, 2017.

Krajewski W.F., G. J. Ciach, and E. Habib, "An analysis of small-scale rainfall variability in different climatic regimes," Hydrological Sci. J., vol. 48, no. 2, pp. 151–162, Apr. 2003, doi:10.1623/hysj.48.2.151.44694.

Kuwayama, Y., Thompson, A., Bernknopf, R., Zaitchik, B. and Vail, P. (2019), Estimating the Impact of Drought on Agriculture Using the U.S. Drought Monitor. American Journal of Agricultural Economics, 101: 193-210. https://doi.org/10.1093/ajae/aay037

Lau, K.M., Yang, S. Climatology and interannual variability of the southeast asian summer monsoon. Adv. Atmos. Sci. 14, 141–162 (1997). https://doi.org/10.1007/s00376-997-0016-y

Lebel, T., A. Diedhiou, and H. Laurent (2003), Seasonal cycle and interannual variability of the Sahelian rainfall at hydrological scales, J. Geophys. Res., 108, 8389, doi:10.1029/2001JD001580.

Leeper, R. D. and Kochendorfer, J.: Evaporation from weighing precipitation gauges: impacts on automated gauge measurements and quality assurance methods, Atmos. Meas. Tech., 8, 2291–2300, https://doi.org/10.5194/amt-8-2291-2015, 2015.

Leitmann-Niimi N., "The changing nature of convection over Earth's tropical oceans from a water budget perspective," M.S. thesis, Dept. Atmos. Sci, Colo. State Univ., Fort Collins, CO, USA, 2023.

Madadgar S., A. AghaKouchak, A. Farahmand, and S. J. Davis (2017), Probabilistic estimates of drought impacts on agricultural production, Geophys. Res. Lett., 44, 7799–7807, doi:10.1002/2017GL073606.

Maggioni, V., M. R. P. Sapiano, and R. F. Adler, 2016: Estimating Uncertainties in High-Resolution Satellite Precipitation Products: Systematic or Random Error?. J. Hydrometeor., 17, 1119–1129, https://doi.org/10.1175/JHM-D-15-0094.1.

Maghsood F.F., H. Hashemi, S. H. Hosseini, and R. Berndtsson, "Ground validation of GPM IMERG precipitation products over Iran," Remote Sens., vol. 12, no. 1, p. 48, Dec. 2019, doi: 10.3390/rs12010048.

Marshall J.S. and W. M. Palmer, "The distribution of raindrops with size," J. Meteorol., vol. 5, pp. 165–166, Jan. 1948, doi: 10.1175/1520-0469(1948)005<0165:TDORWS>2.0.CO;2.

Michaelides S., V. Levizzani, E. Anagnostou, P. Bauer, T. Kasparis, J.E. Lane, Precipitation: Measurement, remote sensing, climatology and modeling, Atmospheric Research, Volume 94, Issue 4, 2009, Pages 512-533, ISSN 0169-8095, https://doi.org/10.1016/j.atmosres.2009.08.017.

Mohr K. I. and E. J. Zipser, "Defining mesoscale convective systems by their 85-GHz ice-scattering signatures," Bull. Amer. Meteorol. Soc., vol. 77, pp. 1179–1190, 1996, doi: 10.1175/1520-0477(1996)077<1179:DMCSBT>2.0.CO;2.

NASA. (2022). Global Precipitation Measurement (GPM) Mission Algorithm Theoretical Basis Document: GPROF2021 Version 1. [Online]. Available: https://gpm.nasa.gov/sites/default/files/2022-06/ATBD_GPM_V7_GPROF.pdf

Nesbitt, S. W., E. J. Zipser, and D. J. Cecil, 2000: A Census of Precipitation Features in the Tropics Using TRMM: Radar, Ice Scattering, and Lightning Observations. J. Climate, 13, 4087–4106, https://doi.org/10.1175/1520-0442(2000)013<4087:ACOPFI>2.0.CO;2.

Nguyen-Le, D., J. Matsumoto, and T. Ngo-Duc, 2015: Onset of the Rainy Seasons in the Eastern Indochina Peninsula. J. Climate, 28, 5645–5666, https://doi.org/10.1175/JCLI-D14-00373.1.

Nicholson, S.E. (2022). The Rainfall and Convective Regime over Equatorial Africa, with Emphasis on the Congo Basin. In Congo Basin Hydrology, Climate, and Biogeochemistry (eds R.M. Tshimanga, G.D.M. N'kaya and D. Alsdorf). https://doi.org/10.1002/9781119657002.ch3

Nielsen, E. R., and R. S. Schumacher, 2020: Dynamical Mechanisms Supporting Extreme Rainfall Accumulations in the Houston “Tax Day” 2016 Flood. Mon. Wea. Rev., 148, 83–109, https://doi.org/10.1175/MWR-D-19-0206.1.

Olson W.S. and GPM CORRA Team. GPM Combined RadarRadiometer Precipitation Algorithm Theoretical Basis Document (Version 7). Accessed: Oct. 7, 2024. [Online]. Available: https://gpm.nasa.gov/sites/default/files/2023-01/Combined_algorithm_ATBD.V07_0.pdf

Petersen, W.A., Kirstetter, PE., Wang, J., Wolff, D.B., Tokay, A. (2020). The GPM Ground Validation Program. In: Levizzani, V., Kidd, C., Kirschbaum, D., Kummerow, C., Nakamura, K., Turk, F. (eds) Satellite Precipitation Measurement. Advances in Global Change Research, vol 69. Springer, Cham. https://doi.org/10.1007/978-3-030-35798-6_2

Petkovic V. and C. D. Kummerow, “Understanding the sources of satellite passive microwave rainfall retrieval systematic errors over land," J. Appl. Meteorol. Climatol., vol. 56, no. 3, pp. 597–614, Mar. 2017, doi: 10.1175/jamc-d-16-0174.1.

Pfreundschuh S., P. J. Brown, C. D. Kummerow, P. Eriksson, and T. Norrestad, "GPROF-NN: A neural-network-based implementation of the Goddard profiling algorithm," Atmos. Meas. Techn., vol. 15, no. 17, pp. 5033–5060, Sep. 2022, doi: 10.5194/amt-15-5033-2022.

Pfreundschuh S., C. Guilloteau, P. J. Brown, C. D. Kummerow, and P. Eriksson, "GPROF V7 and beyond: Assessment of current and potential future versions of the GPROF passive microwave precipitation retrievals against ground radar measurements over the continental US and the Pacific ocean," Atmos. Meas. Techn., vol. 17, no. 2, pp. 515–538, Jan. 2024, doi: 10.5194/amt-17-515-2024.

Pielke, R. A., and M. W. Downton, 2000: Precipitation and Damaging Floods: Trends in the United States, 1932–97. J. Climate, 13, 3625–3637, https://doi.org/10.1175/1520-0442(2000)013<3625:PADFTI>2.0.CO;2.

Raia, A., and I. F. A. Cavalcanti, 2008: The Life Cycle of the South American Monsoon System. J. Climate, 21, 6227–6246, https://doi.org/10.1175/2008JCLI2249.1.

Rehbein A, Ambrizzi T, Mechoso CR, Espinosa SAI, Myers TA. Mesoscale convective systems over the Amazon basin: The GoAmazon2014/5 program. Int J Climatol. 2019; 39: 5599–5618. https://doi.org/10.1002/joc.6173

Richardson, D., Black, A.S., Irving, D. et al. Global increase in wildfire potential from compound fire weather and drought. npj Clim Atmos Sci 5, 23 (2022). https://doi.org/10.1038/s41612-022-00248-4

Ryu G.-H., B.-J. Sohn, C. D. Kummerow, E.-K. Seo, and G. J. Tripoli, "Rain-rate characteristics over the Korean peninsula and improvement of the Goddard profiling (GPROF) database for TMI rainfall retrievals," J. Appl. Meteorol. Climatol., vol. 51, no. 4, pp. 786–798, Apr. 2012, doi: 10.1175/jamc-d-11-094.1.

Sato, K., H. Okamoto, M. K. Yamamoto, S. Fukao, H. Kumagai, Y. Ohno, H. Horie, and M. Abo (2009), 95-GHz Doppler radar and lidar synergy for simultaneous ice microphysics and in-cloud vertical air motion retrieval, J. Geophys. Res., 114, D03203, doi:10.1029/2008JD010222.

Schiro, K. A., S. C. Sullivan, Y. Kuo, H. Su, P. Gentine, G. S. Elsaesser, J. H. Jiang, and J. D. Neelin, 2020: Environmental Controls on Tropical Mesoscale Convective System Precipitation Intensity. J. Atmos. Sci., 77, 4233–4249, https://doi.org/10.1175/JAS-D-20-0111.1.

Schulte, R. M., Chase, R. J., Dolan, B., Marinescu, P. J., Posselt, D. J., Rasmussen, K. L., & van den Heever, S. C. (2024). Unclouding the correlations: A principal component analysis of convective environments. Geophysical Research Letters, 51, e2024GL111732. https://doi.org/10.1029/2024GL111732

Simpson, J., Kummerow, C., Tao, W.K. et al. On the Tropical Rainfall Measuring Mission (TRMM). Meteorl. Atmos. Phys. 60, 19–36 (1996). https://doi.org/10.1007/BF01029783

Smith T.M., P. A. Arkin, J. J. Bates, and G. J. Huffman, "Estimating bias of satellite-based precipitation estimates," J. Hydrometeorol., vol. 7, no. 5, pp. 841–856, Oct. 2006, doi: 10.1175/jhm524.1.

Smola, A.J., Schölkopf, B. A tutorial on support vector regression. Statistics and Computing 14, 199–222 (2004). https://doi.org/10.1023/B:STCO.0000035301.49549.88

Spencer, R. W. (1986). A Satellite Passive 37-GHz Scattering-based Method for Measuring

Oceanic Rain Rates. Journal of Climate and Applied Meteorology, 25(6), 754–766. http://www.jstor.org/stable/26182540

Steiner M., James A Smith, Convective versus stratiform rainfall: An ice-microphysical and kinematic conceptual model, Atmospheric Research, Volumes 47–48, 1998, Pages 317-326, https://doi.org/10.1016/S0169-8095(97)00086-0.

Stephens, G. L., and C. D. Kummerow, 2007: The Remote Sensing of Clouds and Precipitation from Space: A Review. J. Atmos. Sci., 64, 3742–3765, https://doi.org/10.1175/2006JAS2375.1.

Strangeways, I. (2010), A history of rain gauges. Weather, 65: 133-138. https://doi.org/10.1002/wea.548

Tan, J., C. Jakob, and T. P. Lane, 2013: On the Identification of the Large-Scale Properties of Tropical Convection Using Cloud Regimes. J. Climate, 26, 6618–6632, https://doi.org/10.1175/JCLI-D-12-00624.1.

Tan, J., N. Cho, L. Oreopoulos, and P. Kirstetter, 2022: Evaluation of GPROF V05 Precipitation Retrievals under Different Cloud Regimes. J. Hydrometeor., 23, 389–402, https://doi.org/10.1175/JHM-D-21-0154.1.

Tapiador F.J., F.J. Turk, Walt Petersen, Arthur Y. Hou, Eduardo García-Ortega, Luiz A.T. Machado, Carlos F. Angelis, Paola Salio, Chris Kidd, George J. Huffman, Manuel de Castro, Global precipitation measurement: Methods, datasets and applications, Atmospheric Research, Volumes 104–105, 2012, Pages 70-97, ISSN 0169-8095, https://doi.org/10.1016/j.atmosres.2011.10.021.

Tian, Y., and C. D. Peters-Lidard (2010), A global map of uncertainties in satellite-based precipitation measurements, Geophys. Res. Lett., 37, L24407, doi:10.1029/2010GL046008.

Tian, J., X. Dong, B. Xi, J. Wang, C. R. Homeyer, G. M. McFarquhar, and J. Fan (2016), Retrievals of ice cloud microphysical properties of deep convective systems using radar measurements, J. Geophys. Res. Atmos., 121, 10,820–10,839, doi:10.1002/2015JD024686.

Toracinta E. R., D. J. Cecil, E. J. Zipser, and S. W. Nesbitt, “Radar, passive microwave, and lightning characteristics of precipitating systems in the tropics,” Monthly Weather Rev., vol. 130, no. 4, pp. 802–824, Apr. 2002, doi: 10.1175/1520-0493(2002)130<0802:RPMALC>2.0.CO;2.

Villarini G., P. V. Mandapaka, W. F. Krajewski, and R. J. Moore, “Rainfall and sampling uncertainties: A rain gauge perspective,” J. Geophys. Res., Atmos., vol. 113, no. 11, Jun. 2008, doi: 10.1029/2007jd009214.

Vivekanandan, J., J. Turk, and V. N. Bringi, 1991: Ice Water Path Estimation and Characterization Using Passive Microwave Radiometry. J. Appl. Meteor. Climatol., 30, 1407–1421, https://doi.org/10.1175/1520-0450(1991)030<1407:IWPEAC>2.0.CO;2.

Vivekanandan J., D. N. Yates, and E. A. Brandes, “The influence of terrain on rainfall estimates from radar reflectivity and specific propagation phase observations,” J. Atmos. Ocean. Technol., vol. 16, no. 7, pp. 837–845, Jul. 1999, doi: 10.1175/1520-0426(1999)016<0837:TIOTOR>2.0.CO;2.

Wang Z. and C.-P. Chang, “A numerical study of the interaction between the large-scale monsoon circulation and orographic precipitation over South and Southeast Asia,” J. Climate, vol. 25, no. 7, pp. 2440–2455, Apr. 2012, doi: 10.1175/jcli-d-11-00136.1.

Wilheit, T. T., 1986: Some Comments on Passive Microwave Measurement of Rain. Bull. Amer. Meteor. Soc., 67, 1226–1232, https://doi.org/10.1175/1520-0477(1986)067<1226:SCOPMM>2.0.CO;2.

Wright, D. B., D. B. Kirschbaum, and S. Yatheendradas, 2017: Satellite Precipitation Characterization, Error Modeling, and Error Correction Using Censored Shifted Gamma Distributions. J. Hydrometeor., 18, 2801–2815, https://doi.org/10.1175/JHM-D-17-0060.1.

You Y., G. Liu, Y. Wang, and J. Cao, “On the sensitivity of tropical rainfall measuring mission (TRMM) microwave imager channels to overland rainfall,” J. Geophys. Res., vol. 116, Jun. 2011, doi: 10.1029/2010JD015345.

Zhang F. and L. J. O'Donnell, Chapter 7 - Support vector regression, Editor(s): Andrea Mechelli, Sandra Vieira, Machine Learning, Academic Press, 2020, Pages 123-140, ISBN 9780128157398, https://doi.org/10.1016/B978-0-12-815739-8.00007-9.

Zhang, J., and Coauthors, 2016: Multi-Radar Multi-Sensor (MRMS) Quantitative Precipitation Estimation: Initial Operating Capabilities. Bull. Amer. Meteor. Soc., 97, 621–638, https://doi.org/10.1175/BAMS-D-14-00174.1.

Zipser, E. J., D. J. Cecil, C. Liu, S. W. Nesbitt, and D. P. Yorty, 2006: WHERE ARE THE MOST INTENSE THUNDERSTORMS ON EARTH?. Bull. Amer. Meteor. Soc., 87, 1057–1072, https://doi.org/10.1175/BAMS-87-8-1057.